

Sustainable functionalized smectitic clay-based nano hydrated zirconium oxides for enhanced levofloxacin sorption from aqueous medium

Maged Ali, Elgarahy Ahmed M., Haneklaus Nils H., Gupta Ashok Kumar, Show Pau-Loke, Bhatnagar Amit

This is a Publisher's version
published by Elsevier
in Journal of Hazardous Materials
version of a publication

DOI: 10.1016/j.jhazmat.2023.131325

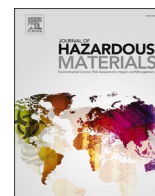
Copyright of the original publication:

© 2023 The Author(s). Published by Elsevier B.V.

Please cite the publication as follows:

Maged, A., Elgarahy, A.M., Haneklaus, N.H., Gupta, A.K., Show, P., Bhatnagar, A. (2023). Sustainable functionalized smectitic clay-based nano hydrated zirconium oxides for enhanced levofloxacin sorption from aqueous medium. Journal of Hazardous Materials, vol. 452. DOI: 10.1016/j.jhazmat.2023.131325

**This is a parallel published version of an original publication.
This version can differ from the original published article.**



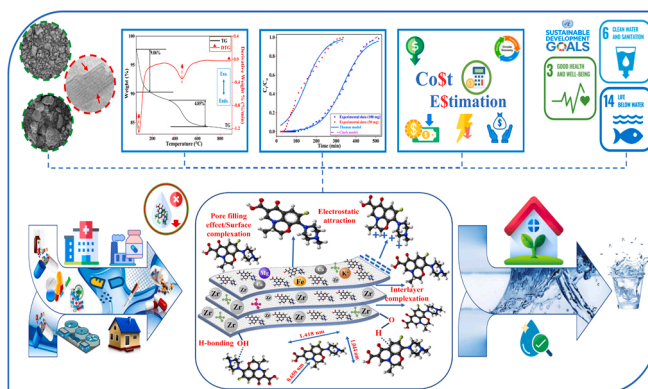
Sustainable functionalized smectitic clay-based nano hydrated zirconium oxides for enhanced levofloxacin sorption from aqueous medium

Ali Maged^{a,b,*}, Ahmed M. Elgarahy^{c,d}, Nils H. Haneklaus^{e,f}, Ashok Kumar Gupta^g,
Pau-Loke Show^{h,i}, Amit Bhatnagar^a

ⁱ Department of Sustainable Engineering, Saveetha School of Engineering, SIMATS, 602105 Chennai, India

GRAPHICAL ABSTRACT

- $\text{ZrO}(\text{OH})_2$ nanoparticles were successfully impregnated into the smectitic clay.
- The synthesized ZrO-SC exhibits excellent stability in strongly acidic medium.
- The ZrO-SC surface area increased more than six-fold after ZrO impregnation.
- Complete mechanistic study of LVN sorption by ZrO-SC was successfully provided.
- Cost estimation and economic evaluation of SC and ZrO-SC were precisely presented.



ABSTRACT

Cost estimation

In this study, the functionalized smectitic clay (SC)-based nanoscale hydrated zirconium oxide (ZrO-SC) was successfully synthesized and utilized for the adsorptive removal of levofloxacin (LVN) from an aqueous medium. The synthesized ZrO-SC and its precursors (SC and hydrated zirconium oxide (ZrO(OH)₂)) were extensively characterized using various analytical methods to get insight into their physicochemical properties. The results of stability investigation confirmed that ZrO-SC composite is chemically stable in strongly acidic medium. The surface measurements revealed that ZrO impregnation to SC resulted in an increased surface area (six-fold higher than SC). The maximum sorption capacity of ZrO-SC for LVN was 356.98 and 68.87 mg g⁻¹ during batch and continuous flow mode studies, respectively. The mechanistic studies of LVN sorption onto ZrO-SC revealed that

E-mail addresses: Ali.Maged@suezuni.edu.eg, Ali.Gharieb@lut.fi (A. Maged).

various sorption mechanisms, such as interlayer complexation, π - π interaction, electrostatic interaction, and surface complexation were involved. The kinetic studies of ZrO-SC in the continuous-flow mode indicated the better applicability of Thomas model. However, the good fitting of Clark model suggested the multi-layer sorption of LVN. The cost estimation of the studied sorbents was also assessed. The obtained results indicate that ZrO-SC is capable of removing LVN and other emergent pollutants from water at a reasonable cost.

1. Introduction

Water is a critical component in attaining United Nation's Sustainable Development Goals (SDGs). Clean and accessible water is essential for the daily lives of people, as well as for the production of food, energy, and goods. Various antibiotic residues and their metabolites have been detected in freshwater resources, which are discharged from hospitals, pharmaceutical industries, and via human excretion [3,30]. Despite being necessary in many human and veterinary medicine practices, antibiotics can be hazardous to the environment when released into natural water bodies, even at low concentrations [96]. Levofloxacin (LVN), a member of the fluoroquinolone antibiotic class, is a broad-spectrum antibacterial drug, used to treat severe bacterial infections [105]. LVN is one of the most widely consumed antibiotics in the world, with an estimated 1.6 billion doses being used yearly [43]. LVN exhibits a high degree of excretion of unmetabolized molecules into the environment via wastewater treatment plants, compared to other antibiotics [68]. Furthermore, the low biodegradability and high hydrophilicity ($\log_{\text{KOW}} = -0.39$) of LVN render it challenging to eliminate it from wastewater through conventional treatment processes such as biological methods [41]. Therefore, developing an effective and successful remediation process to eliminate LVN from aquatic environments is urgently essential.

Various methods have been utilized in the removal of LVN from aqueous solution such as electrochemical treatment [111], nano-filtration [19], photocatalytic degradation [35], advanced oxidation processes [54,108], adsorption [76], sonocatalytic degradation [95], and thermosensitive flocculant [86]. Moreover, some of these methods have been combined and employed to ensure the efficient elimination of LVN from wastewater, such as adsorption/membrane processes [92], photo-catalytic degradation/adsorption [36], sono-photocatalytic hybrid process [30], and advanced oxidation/adsorption [25]. Amidst these methods, adsorption is considered a promising applied technique in water treatment due to its ease of use, economic viability, and ability to eliminate a broad range of noxious compounds from water [70,101].

Therefore, numerous nano/microstructure materials either as single phase or composites have been examined as potential adsorbents for effective removal of LVN from water, including activated charcoal [98], mesoporous iron oxide nanoparticles [67], activated biochar [56], metal organic frameworks [15], pencil graphite/ Fe_3O_4 nanoparticles [6,38], nano-titanium/bentonite composite [60], cellulose/graphene oxide composite [87], zinc oxide/silica nanocomposite [2], iron-pillared montmorillonite [51], and clay minerals [31,99]. Nanoscale hydrated zirconium oxide ($\text{ZrO}(\text{OH})_2$) and this material-based synthetic structures have been widely exploited as effective adsorbents owing to their advantageous characteristics, such as stability over a wide pH range, voluminous surface area, and enormous hydroxyl groups [49]. However, the small size of $\text{ZrO}(\text{OH})_2$ particles makes it difficult to separate them from wastewater after adsorption, resulting in its difficult utilization for practical applications in the treatment process [77]. $\text{ZrO}(\text{OH})_2$ can be permeated onto porous raw material to address this issue, thereby improving its separation from contaminated water and enhancing its adsorption capacity. Consequently, an abundant low-cost carrier/supporter with an easy separation and reusability method should be identified to enable the impregnation of $\text{ZrO}(\text{OH})_2$ particles. Therefore, clays, specifically SC, are considered as the superior candidate for this purpose.

SC is a low-cost and abundant material (2:1 type layered-structure

clay mineral). SC has a high surface area and can form stable complexes with pollutants owing to the presence of exchangeable ions within the original structure, making it effective for removing toxic pollutants [29]. SC is also relatively easy to separate from wastewater after adsorption, making it suitable for reuse. SC is a highly suitable material for modification and intercalation, as it can remain in its original form even after modification [33]. Moreover, the clay structure allows for the insertion of molecules between the layers without altering the original structure [13]. Therefore, the use of nano $\text{ZrO}(\text{OH})_2$ particles and low-cost SC composite combines the fields of nano-science and environmental technology to bring a turning point in water treatment processes.

The present study reports the successful synthesis of a novel ZrO-SC sorbent via a simple and cost-effective ion exchange-precipitation method. This study intended to enhance the sorption capacity of the low-cost SC towards fluoroquinolone antibiotic, specifically LVN, in both surface and interlayer spaces using hydrated zirconium oxide ($\text{ZrO}(\text{OH})_2$). The stability test of ZrO-SC was successfully performed, and the appropriate amount of $\text{ZrO}(\text{OH})_2$ was carefully adjusted. The prepared ZrO-SC and the original precursors (SC and $\text{ZrO}(\text{OH})_2$) were intensively characterized via various analytical methods. The thermal stability and endo/exo-thermic variations of ZrO-SC and its precursors were conducted via the thermogravimetry differential thermal (TG-DTA) measurements. The accurate determination of SC's original and expanded interlayer space was achieved and proved via X-ray diffraction (XRD) and transmission electron microscopy (TEM) analysis. The SC and ZrO-SC sorbents were utilized for LVN sorption from aqueous solutions via two sorption modes (batch and continuous fixed bed column mode). The impact of various experimental/environmental conditions and parameters was also tested in the utilized adsorption modes. Various isotherm and kinetic models for the employed sorption systems were applied. Moreover, the regeneration possibility of ZrO-SC was effectively evaluated. Additionally, the possible sorption mechanisms of LVN on SC and ZrO-SC were also successfully investigated. Finally, cost estimation and an economic assessment of the utilized sorbents is briefly presented.

2. Materials and methods

2.1. Clay samples

Natural smectitic clay (SC) samples were collected from Matrouh governorate (Al-Hammam area), Egypt. The SC samples were crushed, pulverized, separated, and sieved ($\leq 80 \mu\text{m}$). Thereafter, SC samples were washed (Milli-Q water) and dried before the required pretreatment. The reagents and characterization techniques (methodology and instrumentation) utilized in this study can be found in the [supplementary material \(Sections S1–2\)](#).

2.2. Preparation of SC, $\text{ZrO}(\text{OH})_2$, and ZrO-SC

For the pretreatment of SC sample, 50 g of SC was immersed in a 700 mL buffer solution (sodium acetate (0.1 N) and acetic acid solution) to get rid of the existing carbonates, followed by gradual addition of H_2O_2 (ca. $\approx 100 \text{ mL}$) to eradicate organic matter. Then, the mixed slurry (SC and solution) was stirred for 12 h at $60 \pm 1^\circ\text{C}$, followed by 12 h at $25 \pm 1^\circ\text{C}$. Thereafter, the slurry was kept without stirring to settle down. Subsequently, the suspension was centrifuged, filtered, washed (few times by NaCl solution (0.05 N)), and dried ($100 \pm 1^\circ\text{C}$, air oven, 24 h).

Afterward, the SC sample was milled, sieved (40 mesh), and kept in a glass vial for further experiments.

For synthesizing ZrO-SC adsorbent, the ion exchange-precipitation method was utilized to fabricate the desired sorbent. Briefly, 200 mg of $\text{ZrOCl}_2 \cdot 0.8 \text{H}_2\text{O}$ (zirconium dichloride oxide octahydrate) was initially disbanded in 200 mL of 30.0% ethanol solution with a low stirring speed (50 rpm) for 60 min. Next, 400 mg of SC was gradually added to the prepared solution while stirring at 150 rpm (magnetic stirrer at $50 \pm 1^\circ\text{C}$) for 12 h. The SC was carefully poured into 50 mL tubes and centrifuged until all liquid was removed. After careful filtration, the SC particles were added to 150 mL of alkaline solution (NaOH, 5.0 wt%) to start the precipitation reaction. Thereafter, the suspended material was centrifuged and filtered, followed by rinsing with Milli-Q water. This step was conducted multiple times until neutral pH was achieved. Lastly, the obtained composite was dried (spread horizontally in a petri dish) at $70 \pm 1^\circ\text{C}$ for 14 h and, then milled, sieved, and stored.

For $\text{ZrO}(\text{OH})_2$ particles, a similar synthesis procedure was used as ZrO-SC, however, SC sample was not added to the zirconium/ethanol solution. The NaOH solution was directly added to the zirconium/ethanol solution. A white precipitate was formed, and $\text{ZrO}(\text{OH})_2$ particles were obtained through centrifugation and neutralized with deionized water.

2.3. Stability test

In order to assess the stability of ZrO-SC, the influence of various solution pH on ZrO-SC was examined. Briefly, 100 mg of ZrO-SC was added to 100 mL of DI water in a capped 200 mL glass bottle. The initial pH of the mixed solution was adjusted to varied pH values (1–10) using HCl and NaOH solutions. The adjusted solutions with ZrO-SC were kept in a shaker (200 rpm) for 24 h at the normal laboratory temperature ($\approx 25^\circ\text{C}$). Thereafter, 15 mL of each shaken solution was withdrawn, and zirconium concentration was quantitatively analyzed employing the inductively coupled plasma mass spectrometry (ICP-MS).

2.4. Batch mode studies

Batch adsorption experiments were conducted using SC and ZrO-SC sorbents to evaluate and compare their ability to remove LVN from aqueous solutions. The experimental details of the batch mode, conditions, and equations are explained in Section S2 (supplementary material). Moreover, the detailed description of the employed theoretical models (kinetic and isotherm), equations, parameters, and references are summarized in Sections S3–4 (supplementary material, Tables S1–2).

2.5. Continuous fixed-bed column studies

The nano $\text{ZrO}(\text{OH})_2$ loaded smectitic clay was further examined in the continuous flow mode to see the practical application of the synthesized material. The fixed-bed column study was conducted using a glass column (130.0 * 5.0 mm, Omnifit™) along with a peristaltic pump to maintain the effluent flow through the fixed bed. Two appropriate glass wool layers were sandwiched the ZrO-SC adsorbent during the experiment to avoid any adsorbent loss. Varied parameters, including flow rates (1.5 and 3.0 mL min^{-1}), effluent concentrations (10.0 and 20.0 mg L^{-1}), and packed ZrO-SC amounts (50.0 and 100.0 mg), were investigated during the column studies. At different time intervals, the effluent samples were collected and analyzed (λ_{max} of 287 nm, UV–vis spectrophotometer). All the column experimental runs were performed in duplicate under identical conditions. Furthermore, the breakthrough curves were plotted to assess the fixed-bed column's adsorption performance (time vs. C_t/C_o) and the fixed-bed parameters were estimated. Section S5 (supplementary material) summarizes detailed information about the applied equations, column parameters, and calculations.

2.5.1. Column kinetic studies

Two well-suited kinetic models (non-linear forms) were applied to the data obtained from various column experimental runs. Thomas model [88], Eq. (1), is widely utilized for predicting the theoretical results of the applied column uptake [18].

$$\frac{C_t}{C_o} = \frac{1}{1 + \exp\left(\frac{k_{Th}q_e m_{ZrO-SC}}{Q} - k_{Th}C_o t\right)} \quad (1)$$

where k_{Th} ($\text{mL min}^{-1} \text{mg}^{-1}$) and q_e (mg g^{-1}) are the model constant and uptake capacity, respectively. m_{ZrO-SC} is the ZrO-SC loading amount inside the column.

Clark model was initially founded, by Clark [17], based on the combination aspect of the mass-transfer concept and Freundlich isotherm model (Eq. (2)).

$$\frac{C_t}{C_o} = \left(\frac{1}{1 + Ae^{-n}}\right)^{\frac{1}{r}} \quad (2)$$

where n is the unitless Freundlich constant. A and r are the unitless Clark model parameters [11,24].

3. Results and discussion

3.1. Stability investigation of ZrO-SC

In order to assess the utilization feasibility of ZrO-SC in varied aquatic conditions, a stability investigation was performed. Fig. 1 (a) demonstrates the impact of solution pH (ranging from 1 to 10) on the stability of ZrO-SC. The results showed that ZrO-SC was slightly impacted under the strong acidic medium ($\text{pH} \approx 1$). The Zr leaching percentage was found to be 0.29 mg L^{-1} at pH 1. However, no Zr leaching was detected from ZrO-SC in pH value more than 1. Moreover, the final pH values were also measured, showing that only a slight increase in pH occurred after the stability test (Fig. 1 (a)). This finding could be assigned to the protonation of the hydroxyl groups that existed on the ZrO-SC surface. Also, these results confirmed that this increase in final pH is not related to the dissolution reaction between ZrO-SC and H^+ . Overall, the conducted experiments and obtained results proved that the synthesized ZrO-SC adsorbent is chemically stable even at a strongly acidic medium ($\text{pH} < 2$). The Zr loading stability of the synthesized ZrO-SC towards LVN was also examined. Fig. 1 (b) illustrates the uptake capacity of ZrO-SC by increasing the concentration of $\text{ZrOCl}_2 \cdot 0.8 \text{H}_2\text{O}$ / 200 mL ethanol solution. The results exhibited that the uptake capacity enhanced with increasing $\text{ZrOCl}_2 \cdot 0.8 \text{H}_2\text{O}$ amount up to

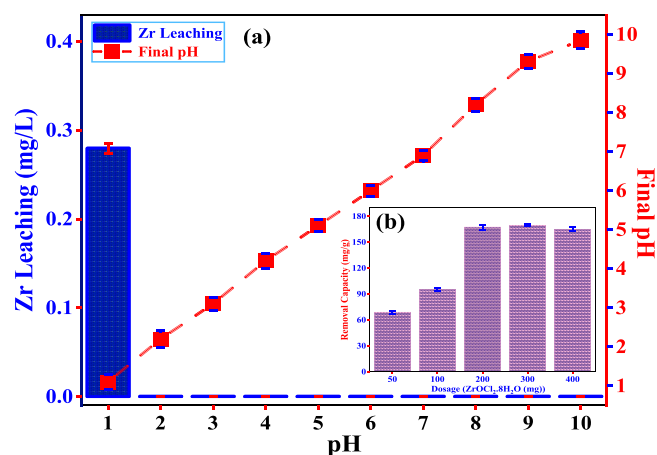


Fig. 1. (a) Leaching of Zr in the solution from ZrO-SC at varied pH range (1–10) with 0.1 g L^{-1} ZrO-SC at 25°C and 200 rpm for 24 h shaking, and (b) Adsorbed amount of LVN onto ZrO-SC prepared with different amounts of $\text{ZrOCl}_2 \cdot 0.8 \text{H}_2\text{O}$ in 200 mL ethanol solution.

200 mg (Fig. 1 (b)). Afterwards, the adsorbed amount of LVN remained almost constant with increasing Zr amounts higher than 200 mg. Nevertheless, an insignificant decrease in the uptake capacity of LVN was noticed with 400 mg dosage of $\text{ZrOCl}_2 \cdot 8 \text{H}_2\text{O}$.

3.2. Characterization studies

3.2.1. X-ray fluorescence (XRF) analysis

The XRF analysis was performed to assess and compare the chemical compositions of SC and ZrO-SC. Table 1 illustrates that SiO_2 and Al_2O_3 were the predominant oxides (wt%) in the studied samples, along with varied Fe, Mg, Ca, Al, K, and Na oxide contents. The $\text{Al}_2\text{O}_3/\text{SiO}_2$ ratio was applied to SC (0.37) and ZrO-SC (0.36) samples, confirming the high existence of the smectite (montmorillonite) mineral in the studied samples. Also, these values indicated that the Zr impregnation did not alter the original structure of the smectitic clay. XRF analysis showed a relatively significant decrease in the oxide weight percentages of Ti (from 0.99 wt% to 0.62 wt%), Fe (from 8.52 wt% to 7.71 wt%), Al (from 20.01 wt% to 18.95 wt%), and Mg (from 2.72 wt% to 1.04 wt%) after the impregnation of hydrated ZrO. However, ZrO weight percentage was increased to 5.23 wt% in ZrO-SC after this impregnation, compared to 0 wt% in SC (Table 1). The results indicated that Zr^{4+} was incorporated into SC through the ion exchange of existing cations (K^+ , Al^{3+} , and Mg^{2+}) in the interlayer spaces of SC during the synthesis process [37]. Consequently, after NaOH addition, $\text{ZrO}(\text{OH})_2$ particles were produced in the final form (ZrO(OH)-SC). Furthermore, relatively high L.O.I. values were found for both SC (10.05 wt%) and ZrO-SC (10.48 wt%). These values could be ascribed to anhydrous material, water, and remaining organic matter content, which were expelled from SC and ZrO-SC during the ignition process.

3.2.2. XRD analysis

The XRD analysis was conducted to assess the variations in the structure layers of SC before and after the Zr impregnation. The XRD patterns of SC, ZrO-SC, and $\text{ZrO}(\text{OH})_2$ nano-particles are demonstrated in Fig. 2(a). The analyzed XRD spectra of SC (raw clay) confirmed the existence of smectite, quartz, and kaolinite minerals in the examined sample. The characteristic peak of smectite mineral was spotted at 2θ value of 6.52° in addition to the presence at 2θ value around 20° [65]. The interlayer spacing of SC at 2θ value of 6.52° was found to be 1.36 nm (calculated according to Bragg's law; Eq. S17). Moreover, the $\text{ZrO}(\text{OH})_2$ spectra (Fig. 2a) revealed that the synthesized particles had an amorphous nature [49], which is practically favorable for LVN adsorption from aqueous medium [46,47]. After impregnating the amorphous nano- $\text{ZrO}(\text{OH})_2$ particles to SC, some changes were recorded in the XRD spectra of ZrO-SC. Generally, the intensity of the characteristic smectite peaks decreased significantly, especially peak (001) at 2θ value of 6.52° . Also, this peak was shifted towards a low 2θ angle at 5.63° . This shift led

Table 1

The chemical composition of SC and ZrO-SC samples (% by weight).

Metal oxide (wt%)	Adsorbent samples	
	SC	ZrO-SC
SiO_2	53.84	52.63
Al_2O_3	20.01	18.95
TiO_2	0.99	0.62
Fe_2O_3	8.52	7.71
MgO	2.72	1.04
CaO	0.73	0.77
K_2O	1.61	1.02
Na_2O	1.44	1.18
P_2O_5	0.09	0.01
ZrO	0.00	5.23
L.O.I.*	10.05	10.84
$\text{Al}_2\text{O}_3/\text{SiO}_2$	0.37	0.36

* L.O.I.= loss on ignition

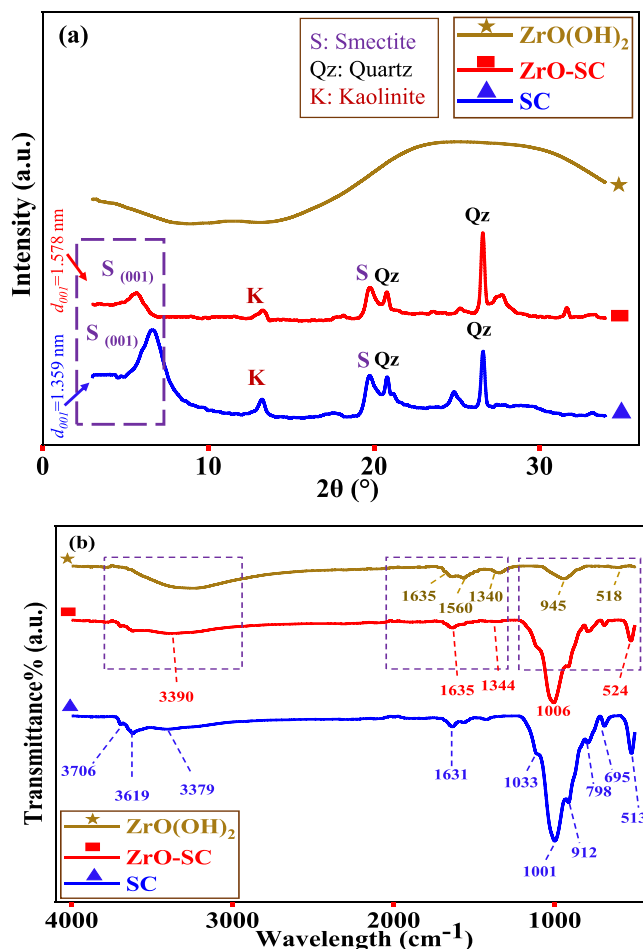


Fig. 2. Characterization results of $\text{ZrO}(\text{OH})_2$, ZrO-SC, and SC samples (a) XRD Pattern ($2\theta = 3\text{--}35^\circ$), (b) FTIR spectra ($400\text{--}4000 \text{ cm}^{-1}$).

to an increase in the interlayer space of ZrO-SC (001 lattice plane), yielding an interlayer spacing of 1.58 nm (d_{001}). The recorded increase in the interlayer layout is ascribed to the intercalated $\text{ZrO}(\text{OH})_2$ nano-particles into SC layer structure. Similar observations were reported on the intercalation of kaolinite [58] and vermiculite [71]. This also explains the substantial increase in the removal capacity of $\text{ZrO}(\text{OH})_2$ toward the targeted pharmaceutical compound, compared to raw clay (SC).

3.2.3. Fourier-transform infrared (FT-IR) analysis

The FT-IR analysis was employed to determine the existing functional groups on the synthesized materials' surface (Fig. 2 (b)). The characteristic smectitic clay bands were detected at 3619, 1001, 912, and 695 cm^{-1} for SC. The FT-IR band appeared at 3379 cm^{-1} could be assigned to H–OH vibrations of the sorbed H_2O molecules on the SC structure. However, the spectral band at 3619 cm^{-1} could be due to the stretching vibration of O–H existed in the silanol groups (Si–OH) of the studied clay sample. The –OH stretching region in SC related to H–OH bond of water molecules was detected at 1631 cm^{-1} [85], which is accompanied by the –OH stretching modes in the silicate matrix (Al (OH)Si groups) [12]. The low-transmittance distributed peaks (SC spectrum), existed between 1300 and 1400 cm^{-1} , are designated to the stretching vibration of other existing metal oxides (Mg–O, Al–O, Fe–O, etc.) [84]. A strong band at 1011 cm^{-1} was noticed in SC spectrum, corresponding to Si–O stretching vibration groups in the tetrahedral layer [44]. Additionally, the band at 902 cm^{-1} is ascribed to Al–Al–OH group of the existing octahedral Al of SC [12]. The bands at 798 and 695 cm^{-1} are assigned to Al–Mg–OH and SiO_2 admixture in

SC, respectively. The weak band around 790 cm^{-1} could be assigned to the Si–O–Fe stretching vibration [113]. The band at 513 cm^{-1} in the SC spectrum could be assigned to the inner bending of –OH group related to SC structure [81]. For ZrO-SC and $\text{ZrO}(\text{OH})_2$ (Fig. 2 (b)), a broad FT-IR band appeared around $\approx 3390\text{ cm}^{-1}$, assigned to –OH stretching vibrations in the H_2O adsorbed-molecules on their surfaces [50]. The OH stretching zone of the inner SC surface had significant changes after the interlayer ad Zr impregnation. The detected variations in this range confirmed the breakdown of the initial hydrogen bonds and consequently formed new hydrogen bonds with the existing surface groups. Furthermore, FT-IR bands at ≈ 518 and 1340 cm^{-1} were detected in $\text{ZrO}(\text{OH})_2$ and ZrO-SC spectrum, which can be assigned to the bending vibrations of Zr–O and Zr–OH, respectively [53]. These findings confirmed the successful impregnation of the nano $\text{ZrO}(\text{OH})_2$ into SC. For ZrO-SC spectrum, the bands at 3706 and 3619 cm^{-1} showed an extensive decrease in the intensity along with slight shifting towards the low wavelength values. Similar effect was also detected in the band at 1001 cm^{-1} in SC, which shifted to 1006 cm^{-1} with a decrease in its intensity. The vibration of Zr–OH reinforced a new band at 1344 cm^{-1} in the ZrO-SC spectrum after the Zr nano particles were intercalated. This finding revealed that Zr molecules were bonded with these existing cationic metals via an ion exchange mechanism (as confirmed by XRF analysis) [84].

3.2.4. TG-DTA analysis

TG-DTA measurements were performed to elucidate the thermo-physical changes across endothermic and exothermic effects. Fig. 3 (a, b, and c) demonstrates the TG-DTA graphs ($30\text{--}1000^\circ\text{C}$) of SC, nano-ZrO ($\text{OH})_2$, and ZrO-SC, respectively. Generally, TG curves of SC display three different regions (high, low, and intermediate temperature) of mass loss. These zones provide valuable information at various temperature ranges in addition to assessing the stability of the studied clays. In this study, the TG curve of SC indicated that the first weight loss was found to be $4.22\text{ wt}\%$ at a temperature of less than 200°C . This weight loss can be credited to the depletion of the adsorbed H_2O molecules in addition to the dehydration of interlayer species in SC sample [55].

However, the first endothermic peak appeared at 54°C in the DTA curve (Fig. 3 (a)). Thereafter, the second mass loss was found to be $2.14\text{ wt}\%$ at a temperature range of $200\text{--}400^\circ\text{C}$, attributed to the dehydroxylation reaction of SC [63]. Two endothermic peaks existed in the same temperature region during the dehydroxylation reaction. However, an exothermic peak appeared at 360°C in the DTA curve, which could be ascribed to the oxidation (burn-down) of the remaining organic matter [74]. Subsequently, the third phase of the weight loss was found to be $6.31\text{ wt}\%$ at a temperature range of $400\text{--}760^\circ\text{C}$, corresponding with the endothermic peak at 500°C due to a dehydroxylation reaction in SC. Also, this endothermic peak could be due to calcite's de-carbonation reaction [90]. Further, no weight loss was detected at a temperature of more than 760°C . Fig. 3 (b) demonstrates the TG-DTA curve of the nano- $\text{ZrO}(\text{OH})_2$, showing that one endothermic peak (at 81°C ; DTA) was noticed with a total mass loss of $31.12\text{ wt}\%$ up to 230°C , and no further changes occurred beyond this temperature. Fig. 3 (c) shows the TG-DTA curve of the SC after the impregnation of $\text{ZrO}(\text{OH})_2$ nanoparticles. The thermal analysis indicated that the impregnation of Zr particles to SC caused a significant variation in the TG-DTA curves, compared to the raw SC sample. The TG curve of ZrO-SC revealed that the first weight loss was $9.06\text{ wt}\%$ at a temperature less than 200°C (dehydration effect), accompanied by the appearance of the first endothermic peak at 90°C . The second mass loss was detected in the temperature up to 700°C and found to be $4.85\text{ wt}\%$. Moreover, the endothermic peak at 460°C could be attributed to the dihydroxylation reaction. This endothermic peak shifted to a lower temperature value compared to SC. This phenomenon confirms that the loaded (intercalated) Zr particles influenced the –OH groups of the SC octahedral layer. This could be ascribed to the protonation/dissociation of the existing structural groups of SC after the reaction of the prepared $\text{ZrOCl}_2 \cdot 0.8\text{ H}_2\text{O}$ solution, resulted in the release of some metal ions (i.e., Mg, Fe, Al) from the octahedral layer [9,62]. Comparing the total mass loss indicates that ZrO-SC has a slightly higher total weight loss ($13.91\text{ wt}\%$) compared to SC ($12.49\text{ wt}\%$). This difference is owed to the gained moisture during the preparation of ZrO-SC. Overall, the obtained analysis indicated that SC impregnation by Zr particles significantly enhanced the stability of

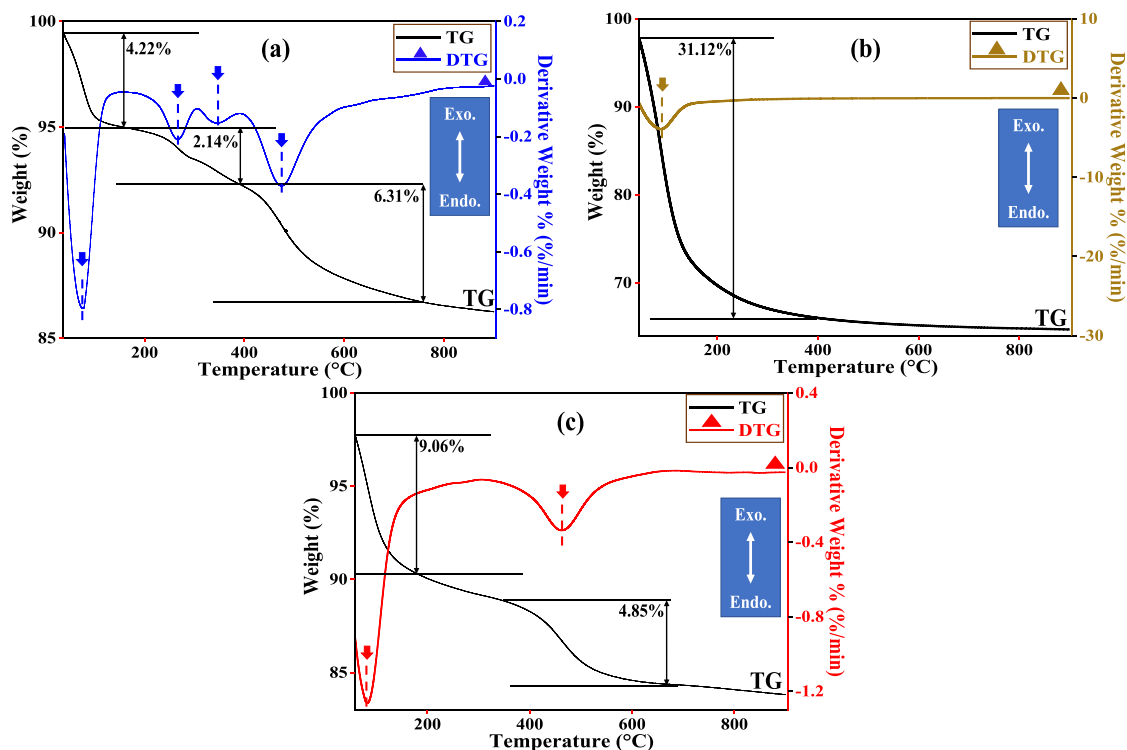


Fig. 3. TG-DTA analysis of (a) SC, (b) $\text{ZrO}(\text{OH})_2$, and (c) ZrO-SC samples.

ZrO-SC.

3.2.5. Textural analysis

Table 2 summarizes the textural assessment of SC and ZrO-SC based on the N_2 adsorption-desorption isotherms. The Brunauer-Emmett-Teller (BET) measurements showed that the synthesized nano ZrO(OH)₂ particles possess a relatively high specific surface area ($434.62 \text{ m}^2 \text{ g}^{-1}$) (Table 2). Moreover, the obtained data illustrated that the impregnation of ZrO(OH)₂ particles into SC considerably improved the specific surface area of SC from 21.63 to $141.55 \text{ m}^2 \text{ g}^{-1}$ (ZrO-SC). This substantial increase can be ascribed to the successful impregnation of ZrO nano particles, which have high specific surface area ($434.62 \text{ m}^2 \text{ g}^{-1}$), into SC. Similar observations to the remarkable increase in the surface area were reported previously when researchers studied the loading of nano particles to various clays [45,66,79]. On the contrary, other parameters, such as total pore volume and mean pore diameter, were considerably decreased (Table 2). The reduced pore properties can be explained due to the blockage of the loaded ZrO(OH)₂ particles onto SC. These results also confirm the successful impregnation of ZrO particles into SC.

3.2.6. FE-SEM-EDX and TEM analysis

The morphological (internal and external) characteristics and chemical composition of SC, ZrO-SC, and ZrO(OH)₂ particles were investigated and verified via TEM and FE-SEM-EDX analysis. Fig. 4(a) shows the amorphous structure of the synthesized Zr particles within a particle size of $10\text{--}40 \text{ nm}$ (confirmed from TEM image (Fig. 4(b)), in addition to the accumulation of ZrO(OH)₂ particles, forming large-sized particles. Moreover, EDX analysis evidently displays the presence of Zr and O in the studied sample (Fig. 4 (c)). However, the naturally occurring SC particles were found in the form of flakes (fractured) with varied sizes and shapes (Fig. 4 (d and e)). The corresponding EDX spectra of SC confirmed that Si, O, and Al are the predominant elemental constituents in SC. Also, the presence of Ti, Na, K, Ca, Fe, and Mg was detected (Fig. 4 (f)). Thereafter, remarkable variations were found after the impregnation of ZrO(OH)₂ particles onto SC (Fig. 4 (g)). The ZrO-SC surface showed more exfoliated sheets compared to SC's existing smooth surface. Fig. 4 (h) proved that ZrO(OH)₂ particles were homogeneously loaded into SC interlayer spacing (dark layer-like structure) without any particle aggregation [58]. Additionally, the EDX spectra of ZrO-SC displayed the presence of Zr ($7.92 \text{ wt}\%$) in its chemical composition with different proportions (wt%) of the other constituents (i.e., Fe, Mg, Na, Al, and Si). This variation could also explain the change of morphology due to the formation of new hydroxyl groups [M-OH (M = Ti, Fe, Zr, and Mg)] on ZrO-SC [42]. Moreover, the existence of Zr particles in the SC structure explains the remarkable elevation in the specific surface area of ZrO-SC (confirmed from BET analysis; Table 2). Moreover, comparing the layer spacing and structure of SC (Fig. 4 (e); blue circle) and ZrO-SC (Fig. 4 (h); red circle) shows that the basal spacing of ZrO-SC was significantly increased after the impregnation of ZrO. These findings indicate that the impregnation method successfully enhanced the ability of SC to capture large molecules (LVN) in the interlayer structure in addition to the active site on the surface.

Table 2

The textural properties of SC and ZrO-SC samples based on N_2 adsorption-desorption isotherms.

Properties	Samples		
	SC	ZrO(OH) ₂	ZrO-SC
Specific Surface Area ($\text{m}^2 \text{ g}^{-1}$)	21.63	434.62	141.55
Total pore volume ($\text{cm}^3 \text{ g}^{-1}$)	0.08	0.29	0.04
Mean pore diameter (nm)	20.11	2.66	13.19
Langmuir surface area ($\text{m}^2 \text{ g}^{-1}$)	27.87	605.47	133.26
BJH surface area ($\text{m}^2 \text{ g}^{-1}$)	21.75	367.29	145.72

3.3. Batch mode adsorption studies

3.3.1. Influence of initial solution pH

Principally, studying the effect of solution pH on the adsorption of any pollutant is critical for optimizing pollutant removal. In addition, the solution pH can also influence the sorbent's surface charge and the pollutant's solubility, which are both crucial factors in the adsorption process. Thus, understanding the solution pH's role in the adsorption of targeted contaminants is essential for efficient pollutant removal. Therefore, the effect of initial pH (pH_i) for the dissolved LVN using SC and Zr-modified SC (ZrO-SC) sorbents was examined by performing experimental sets at different pH_i values ranging from 2 to 9 (Fig. 5). Mostly, the sorption of LVN onto SC, and ZrO-SC fluctuated marginally reliant on the pH_i of the solution. In this regard, the adsorption capacities (mg g^{-1}) and removal efficiency (RE%) were found to be relatively low (38.29 mg g^{-1} , RE% = 67.01%), and (126.71 mg g^{-1} , RE% = 72.40%) at pH_i of 2, and distinctly raised to their utmost values of 53.03 mg g^{-1} (RE% = 90.88%), and 171.43 mg g^{-1} (RE% = 98.03%), for SC, and ZrO-SC, respectively, with regular increment in the pH_i of the solution up to 5.0. Afterward, the adsorption capacities and RE% of the employed sorbents (SC and ZrO-SC) displayed a remarkable decline in the removal of LVN which was 19.75 mg g^{-1} (RE% = 29.29%) and 117.76 mg g^{-1} (RE% = 79.28), respectively, with further increase in the medium pH up to 9.

The LVN sorption onto SC and ZrO-SC can be explained by considering their surface charge values (point of zero charges (pH_{zpc})) and different configurations characters of LVN molecules in terms of the acid dissociative constant (pK_a). Fig. 5(b) shows that the net pH_{zpc} measured values of SC and ZrO-SC sorbents were 4.81 and 5.09, respectively, revealing that, at $pH < pH_{zpc}$, the sorbent surface is positively charged and vice versa [26,28]. Indeed, the acid-base speciation of LVN is zwitterionic, with two pK_a values of 6.02 (pK_{a1}), and 8.15 (pK_{a2}), existing in three different forms of cationic (LVN^+), anionic (LVN^-), and zwitterionic (LVN^\pm) molecules as a function of pH (Fig. 5(d)) [38,98]. Based on pH-dependent speciation, it is noteworthy to clarify that the cationic LVN^+ species exist in the bulk solution when $pK_{a1} < pH < 6.02$, attributing to protonation of amine group on the piperazinyl moiety. While, the anionic LVN^- species are predominantly found at $pK_{a2} > pH = 8.15$, referring to de-protonation of amine and carboxyl binding groups. The non-dissociative (zwitterionic) form of LVN^\pm is readily identified in the region between pK_{a1} , and pK_{a2} [103]. Within the studied solutions, the functional groups of the sorptive sites, present on SC and ZrO-SC sorbents, were prone to be protonated owing to the greater H^+ content under a strongly acidic environment, which in turn strongly hampers the sorption process of cationic LVN^+ species onto the positively charged surfaces of both SC and ZrO-SC (repulsive electrostatic forces) [7]. Moreover, the high concentration of hydronium ions (H_3O^+) could probably compete with LVN^+ to be sorbed on the binding sites of both as-synthesized sorbents, which consequently results in a decrement in their adsorption capacities towards LVN^+ species.

Nonetheless, the non-stoichiometric cation exchange between LVN^+ with the protons of binding groups should be considered [51]. This reaction was supported by the relative change in solution pH during LVN^+ sorption, strongly affirming the replacement of protons with LVN^+ species. Furthermore, the adsorption capacities of SC and ZrO-SC substantially improved with increasing the solution pH_i up to 5.0, recording the highest RE % values of 90.88% and 98.06% for SC and ZrO-SC, respectively, across the broad running pH range (Fig. 5(a, c)). The observable change in the RE% in such conditions can be principally ascribed to the minor content of H^+ and gradual deprotonation of functional groups associated with a slight increase in the electronegativity of the surface of SC and ZrO-SC sorbents, which is beneficial for LVN sorption process (electrostatic attraction forces) [20]. Besides, the sorption of LVN onto SC and ZrO-SC may be promoted by the complex formation between the loaded Zr ions and de-protonated carboxyl

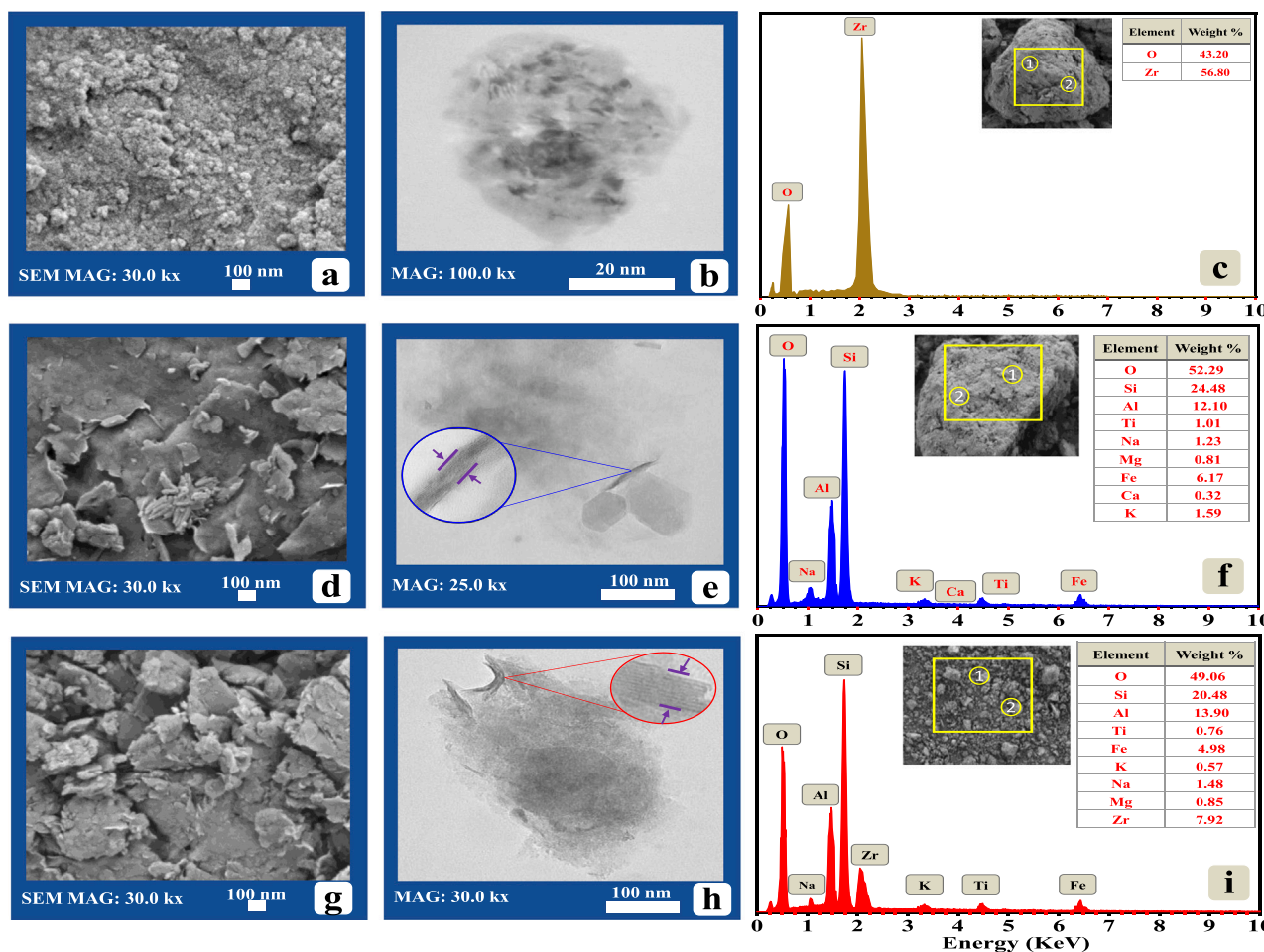


Fig. 4. SEM, TEM, and EDX analysis of: (a, b, and c) $\text{ZrO}(\text{OH})_2$, (d, e, and f) SC, and (g, h, and i) ZrO-SC, respectively.

groups of LVN molecules [107]. Numerous studies have demonstrated that the adsorption capacities of Zr-based materials are strongly pH-dependent [97,110].

On the other hand, the reversible sorption behavior was recorded with continual augmentation in the pH_i value (alkaline region). The dramatic decrease in the adsorption capacities of SC and ZrO-SC can be illustrated by the anionic nature of LVN molecules as they likely get electrostatically repelled by the negatively charged surfaces of SC and ZrO-SC (Fig. 5(a, c)). In other words, OH^- ions are closely associated with the sorptive centers of SC and ZrO-SC under a basic environment. Thereafter, these ions acted as competitor's ions on SC and ZrO-SC surfaces, hindering the LVN sorption process. However, the recorded RE% of SC and ZrO-SC towards LVN under harsh conditions (unfavorable mediums) profoundly deduced that electrostatic interaction was not the sole sorption mechanism. However, there may further be other prevailing mechanisms such as chemical interaction that may influence the sorption process [16]. Overall, the obtained information from pH_{zpc} measurements of the studied adsorbents, LVN speciation, and pH studies of LVN sorption by SC and ZrO-SC significantly assisted in understanding the sorption mechanism, and also confirmed that the Zr modification of SC did not affect the SC behavior under varying pH values.

3.3.2. Influence of sorbent dosage

The amount of sorbent utilized in the sorption process can significantly influence pollutant removal efficiency and the overall process cost. The influence of sorbent concentrations variation (from 0.1 to 1.0 g L^{-1}) on adsorption capacities and RE% of SC and ZrO-SC is shown in Fig. 6(a). It can be seen that the RE% of LVN by ZrO-SC increased from

59.89% to 97.85% at a dosage of 0.2 g L^{-1} . Beyond the ZrO-SC amount of 0.2 g L^{-1} , the LVN sorption reached a plateau state (saturation point) at this particular concentration. However, the RE% of LVN by SC increased from 33.81% to 96.31% without achieving a saturation or plateau state. These findings confirm the superior sorption performance of ZrO-SC compared to SC towards LVN. The notable improvement in the RE% of SC and ZrO-SC sorbents in response to changes in their quantities can be correlated to the initial attainability of different sorptive centers for the sorption. Differently, the uptake capacity of any sorbent is indirectly proportional to its RE% (negative correlation) (Fig. 6 (a)). The noticeable diminution in the SC and ZrO-SC adsorption capacities from 115.14 to 32.80 mg g^{-1} and from 204.00 to 34.06 mg g^{-1} , respectively, with increasing the sorbents concentrations can be explained by the inadequate interaction between LVN molecules with per unit weight of the sorbent [28,106]. Therefore, sorbent amount of 0.2 g L^{-1} was designated as the optimized dosage for LVN removal for both SC and ZrO-SC.

3.3.3. Influence of ionic strength

For affordability and practicality of the adsorbents, ionic strength is also regarded as an essential operational parameter. This parameter modulates the interaction between the sorbent-sorbate interface by altering the thickness of double-layer film and interfacial potential, hence influencing the removal process [108]. Inspecting the RE% index of SC and ZrO-SC sorbents towards LVN in the presence of dissolved background ions to mimic the constituents of industrial wastewater is expedient. NaCl ions were chosen as co-background ions. While the LVN concentration (30 mg L^{-1}) remained constant, various NaCl

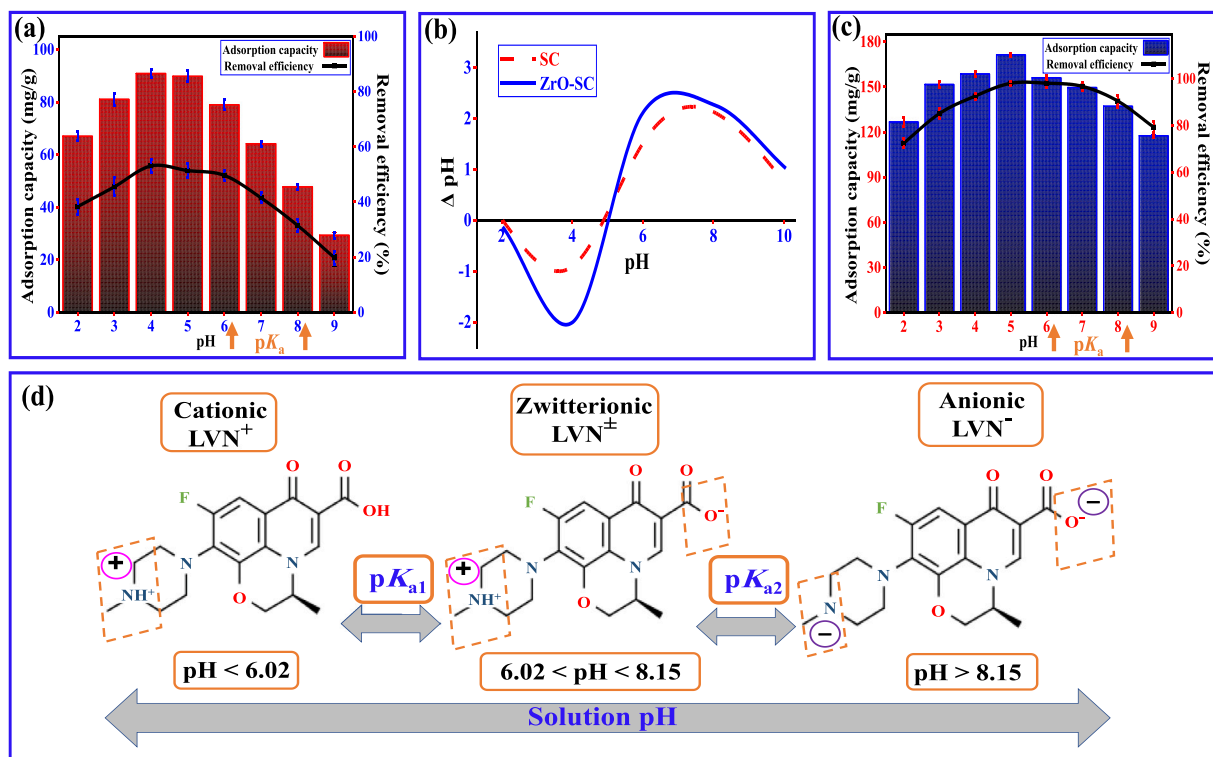


Fig. 5. Mechanism of LVN sorption (a) Effect of pH on LVN sorption using SC, (b) pH_{zpc} measurements of SC and ZrO-SC, (c) Effect of pH on LVN sorption using ZrO-SC, and (d) pH-dependent LVN speciation.

concentrations (0.05–0.25 M) were investigated. As illustrated in Fig. 6 (b), moderate loss in the LVN sorption onto SC and ZrO-SC sorbents was obviously noted in the multi-component system. The variations in the sorption behaviors of LVN onto SC and ZrO-SC are fundamentally attributed to structural and morphological nature differences between the two sorbents. In the case of SC, a noticeable inhibition on the sorption process of SC towards LVN from 51.44% to 13.29% resulted from the competitive ions (Na^+ and Cl^-). This phenomenon could be explained by the possible interaction between the soluble sodium ions (Na^+) and carboxylic groups present in LVN molecular structure to form their sodium salts, which are known to promote the solubilized forms in the targeted solutions than sorption onto the SC and ZrO-SC sorbents [60]. Moreover, Na^+ ions may compete with LVN^+ species to occupy the surface functional groups on the as-employed sorbents [102]. Moreover, compressing the electric double layer (squeezing-out) on the sorbent surface may be promoted over the salting-out phenomenon [56]. Furthermore, as the sorption progressed, the surface area of sorbents was partially reduced due to agglomerates formation between greater NaCl concentrations and sorbents, which in consequence, slumped the LVN removal. Compared to SC, ZrO-SC retained a higher removal efficiency (80.29%) even in a high electrolyte concentration (i.e., 0.25 M), which implied that ZrO-SC is potentially beneficial in the removal of LVN from wastewater, especially brine and industrial wastewater.

3.3.4. Reusability of the spent sorbent

Economically, the stability of as-used sorbent is a critical issue to be addressed, as it strongly supports its industrial applicability via testing its recoverability after the completion of the sorption process. Typically, the adsorption capacity of any sorbent is progressively decreased over time until it becomes saturated. Overall, the beneficial desorption process opens the way to upgrade the sorption process by allowing the sorbate recovery and qualifying the sorbent for further repeated utilization, thus minimizing waste production. In this regard, the recyclability of SC and ZrO-SC was repeatedly inspected to augment the paramount features of the employed sorbent. The optimal conditions for

LVN sorption (0.2 g L⁻¹ (sorbent), 30 mg L⁻¹ (LVN), 25 ± 1 °C), derived from the performed batch experiments, were applied for the initial sorption cycle. Afterwards, two different regeneration agents (HCl and NaOH) were examined as eluents to regenerate the sorptive sites of spent SC and ZrO-SC sorbents. As illustrated in Fig. 6 (c), the adsorption capacities, as well as RE% of the utilized sorbents towards LVN, were strikingly declined under an alkaline environment (using NaOH) from 87.59 mg g⁻¹ (RE% = 51.44%) to 19.46 mg g⁻¹ (RE% = 11.43%), and from 166.64 mg g⁻¹ (RE% = 97.85%) to 53.44 mg g⁻¹ (RE% = 31.38%) for SC and ZrO-SC, respectively, after 7th cycle of sorption-desorption. Contrarily, HCl was found more potent to strip LVN molecules and reactivate the exhausted binding sites of the SC and ZrO-SC sorbents (Fig. 6 (d)). In fact, the regenerated sorbents maintained admirable adsorption capacities (no significant change) of 34.46 and 153.44 mg g⁻¹ for SC and ZrO-SC sorbents, respectively, even after 7th cycle, considering the characteristic adsorption capacities of original sorbents (87.59 and 166.64 mg g⁻¹, for SC and SC-Zr, respectively) (Fig. 6 (d)). This could be due to the protonation of surface charge, resulting in the disruption of sorbed LVN molecules from the sorbent's surface. The comparatively acceptable performance of HCl towards LVN desorption, compared to the less convincing desorption efficiency % (poor treatment) of NaOH, ultimately supposed the contribution of a cation exchange mechanism in the LVN sorption process. The favorable subsequent sorption-desorption findings prioritize HCl as a more preferred contender eluent for LVN desorption and acclaim the reliability of SC and ZrO-SC sorbents through multiple recycling stages.

3.3.5. Kinetic modeling of LVN sorption

The influence of contact time on the sorption profile of LVN onto SC and ZrO-SC sorbents was carried out at varied time intervals to identify the nature of the sorption process. As illustrated in Fig. 7 (a), the obtained data showed that the adsorption capacities of SC and ZrO-SC sorbents sharply increased as a function of time in the first 25 min (fast initial adsorption). The accelerated sorption rate at the beginning of the sorption process was facilitated by the concentration gradient

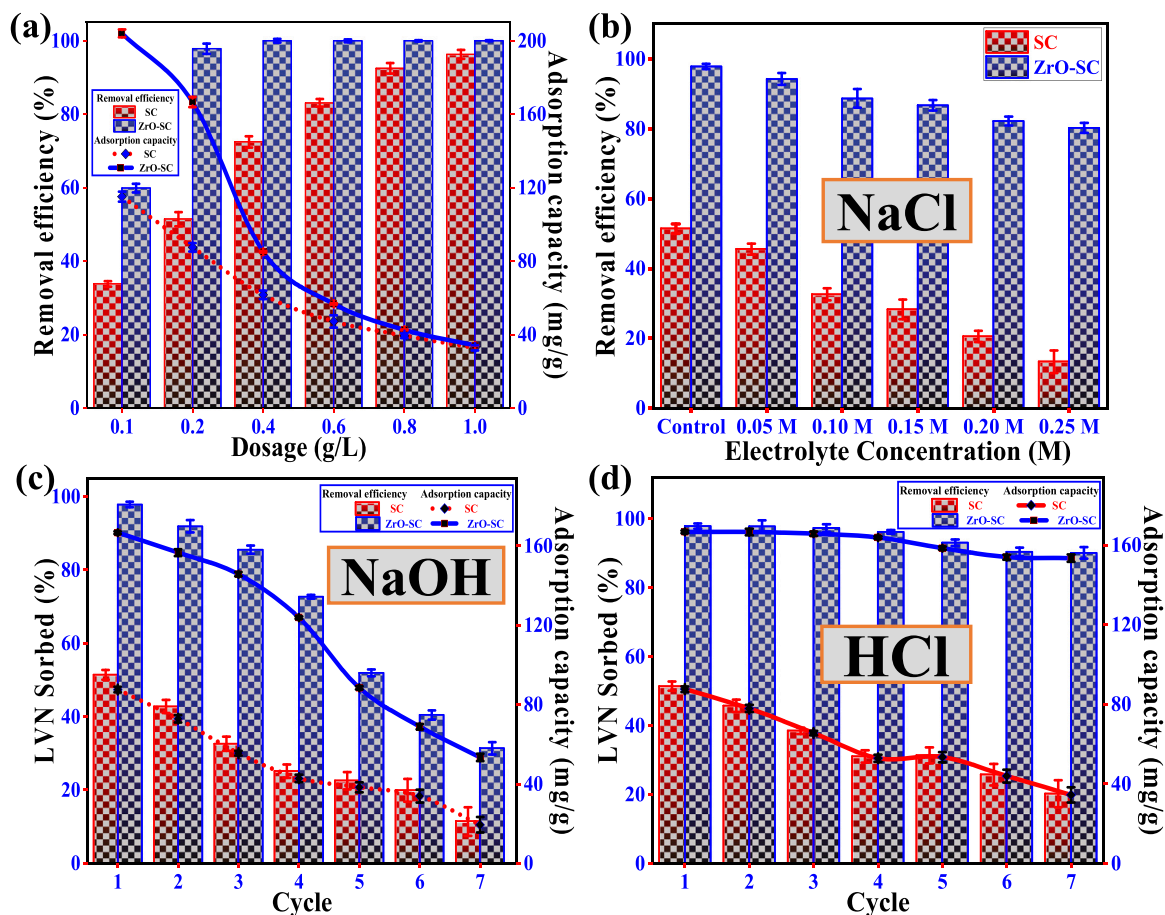


Fig. 6. Effect of (a) adsorbent dosage, (b) ionic strength, regeneration studies using (c) 0.2 M NaOH and (d) 0.2 M HCl as eluent on LVN adsorption using SC and ZrO-SC.

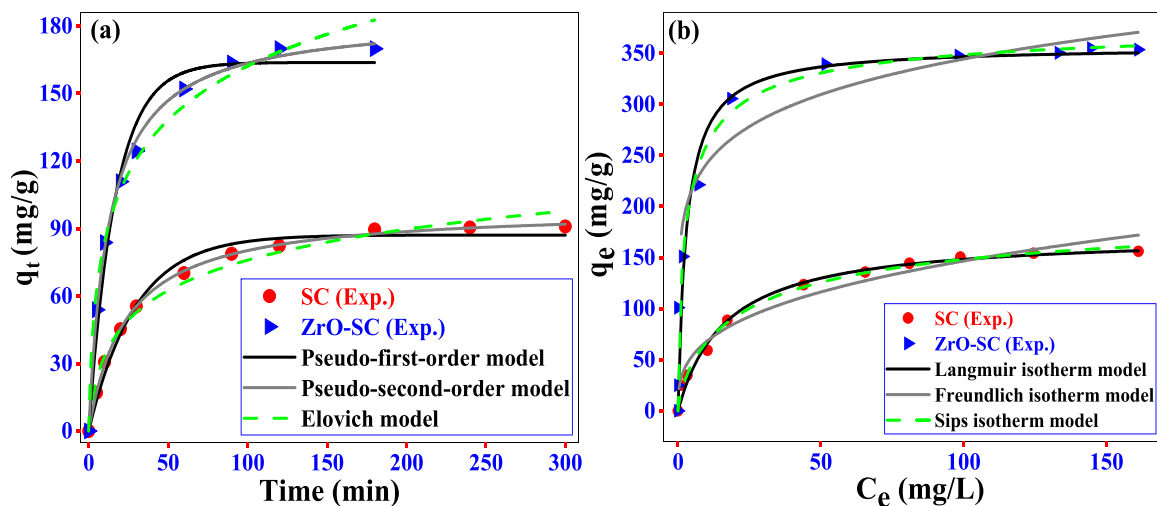


Fig. 7. (a) Non-linear adsorption kinetic modeling of LVN (time: 0–300 min), (b) non-linear adsorption isotherm modeling of LVN (concentration: 10–200 mg L⁻¹) using SC and ZrO-SC.

between the unoccupied sorptive sites and the easily accessed LVN molecules. With increasing the residence time, the sorption rate gradually diminished until stagnant (equilibrium) was attained, and no more sorption occurred.

To further comprehend the experimental findings, the kinetic behavior of LVN sorption by SC and ZrO-SC sorbents was inspected using three standard kinetic models; pseudo-first order, pseudo-second order,

and Elovich. The fitting curves for these models and their calculated parameter values are displayed in Fig. 7(a) and Table 3. In the sorption process of LVN onto SC and ZrO-SC, the pseudo-second-order kinetic model shows a better R^2 (> 0.99) than the pseudo-first-order and Elovich models (Table 3). Obeying the experimental data to the pseudo-second-order model assumes strong chemisorption between the utilized sorbents and LVN molecules (e.g., ion exchange chemical,

Table 3

The model (kinetic and isotherm) parameters of LVN sorption onto SC and ZrO-SC sorbents.

Adsorbent	Kinetic parameters					
Pseudo-first-order model ($q_t = q_e(1 - e^{-k_1 t})$)						
	k_1 (min ⁻¹)	$q_{e,cal}$ (mg g ⁻¹)	$q_{e,exp}$ (mg g ⁻¹)	RMSE	R ²	
SC	0.034	81.08	90.83	3.96	0.984	
ZrO-SC	0.060	161.79	173.87	8.62	0.978	
Pseudo-second-order model ($q_t = \frac{k_2 q_e^2 t}{1 + k_2 q_e t}$)						
	k_2 (g mg ⁻¹ min ⁻¹)	$q_{e,cal}$ (mg g ⁻¹)	$q_{e,exp}$ (mg g ⁻¹)	v_0 (mg g ⁻¹ min ⁻¹)	RMSE	R ²
SC	4.28 E ⁻⁴	96.09	90.83	3.95	0.92	0.999
ZrO-SC	4.26 E ⁻⁴	184.29	173.87	14.47	2.89	0.998
Elovich model ($q_t = (\frac{1}{\beta})Ln(1 + \alpha \beta t)$)						
	α (mg g ⁻¹ min ⁻¹)	β (g min ⁻¹)	$q_{e,exp}$ (mg g ⁻¹)	RMSE	R ²	
SC	8.51	0.049	90.83	7.47	0.982	
ZrO-SC	35.27	0.029	173.87	4.47	0.985	
Isotherm	Langmuir isotherm model ($q_e = \frac{q_m K_L C_e}{1 + K_L C_e}$)					
	$q_{max(cal)}$ (mg g ⁻¹)	K_L (dm ³ mg ⁻¹)	R_L	RMSE	R ²	
SC	172.86	0.06	0.08–0.77	6.17	0.989	
ZrO-SC	356.98	0.33	0.02–0.37	37.15	0.936	
Freundlich isotherm model ($q_e = K_F C_e^{1/n}$)						
	K_F (mg/g)	n	RMSE	R ²		
SC	31.44	2.99	9.59	0.971		
ZrO-SC	169.70	6.51	40.43	0.916		
Sips isotherm model ($q_e = \frac{K_S C_e^{\beta_S}}{1 + a_S C_e^{\beta_S}}$)						
	K_S (L g ⁻¹)	β_S	a_S	RMSE	R ²	
SC	200.32	0.75	0.09	10.09	0.994	
ZrO-SC	356.18	0.69	0.44	37.82	0.941	

complexation, and H-bonding reactions) [3]. Furthermore, the theoretical adsorption capacity based on the pseudo-second-order model was found to be 96.09 and 184.29 mg g⁻¹ for SC and ZrO-SC, respectively, which closely agrees with the experimental value. Moreover, the calculated initial adsorption rate (v_0) showed that ZrO-SC value was found to be four-fold higher compared to SC (Table 3). This finding indicated that loading Zr nanoparticles onto SC noticeably enhanced the removal and sorption rate of LVN.

3.3.6. Isotherms modeling of LVN sorption

The impact of primary LVN concentrations on the sorption performance of SC and ZrO-SC sorbents was evaluated and plotted in Fig. 7 (b). Generally, at low LVN concentrations, the molecules easily diffused through the SC and ZrO-SC sorbents, and rapidly occupied the accessible sorptive sites, exist on their surfaces owing to the weakened steric repulsive forces between the sorbed and diffused LVN molecules. Nevertheless, a similar phenomenon was found at high LVN concentrations through a faster sorption rate. This phenomenon can be elucidated by the fact that there are more LVN molecules than sorptive centers, which exerts a force that drives molecules toward the available localized centers owing to the high-concentration gradient and hence increases the uptake capacity of SC and ZrO-SC sorbents [10,56,57].

The obtained experimental data were fitted to three widely used equilibrium isotherm models (Langmuir, Freundlich, and Sips) using non-linear forms and utilized to assess the LVN sorption onto SC and ZrO-SC sorbents (Fig. 7 (b)). Besides, a summary of the isotherm parameters as a function of initial concentrations is tabulated in Table 3. By inspecting the correlation coefficient (R²) and root mean square error (RMSE) values concerning different isotherm models, the good consistency between Sips model and the experimental data firmly reinforces

its aptness to describe the sorption process. Sips model combines Langmuir and Freundlich models. It is widely employed to forecast the sorption in heterogeneous systems and get beyond the Freundlich isotherm's restriction on higher sorbate concentrations [91]. The results endorsed the governance of LVN sorption by a multi-layer sorption process onto the heterogeneous surface of SC and ZrO-SC sorbents at lower LVN concentrations and monolayer sorption at higher LVN concentrations. Moreover, the calculated K_S , β_S , and a_S for both sorbents at different primary LVN concentrations reflected the favorability of LVN sorption onto SC and ZrO-SC sorbents. Also, the preferability of LVN sorption process was evaluated by considering the dimensionless constant separation factor (R_L) value (Eq. S10; supplementary material). The calculated R_L values for SC and ZrO-SC were found in the range between 0 and 1 (Fig. S1), suggesting that the sorption process is favorable and a strong binding between LVN molecules and the prepared sorbents occurred [27,59]. Furthermore, ZrO-SC showed an increased monolayer sorption capacity of 356.98 mg g⁻¹ compared to SC (172.86 mg g⁻¹). These results indicate that impregnation Zr particles to SC significantly enhanced the LVN sorption for more than two-fold compared to SC.

3.3.7. Performance comparison study

In order to evaluate the potentiality and applicability of the prepared sorbent compared to the other existed adsorbents, the maximum monolayer adsorption capacity (q_{max}) of SC and ZrO-SC for the removal of LVN was compared with of several reported carbonaceous, non-carbonaceous, natural minerals and chemically synthesized adsorbents in the literature (Table S4). The prepared sorbents in this study exhibited a superior adsorption capacity for LVN compared to other carbonaceous adsorbents such Zr-modified CBs [109], activated biochar [56], supported pencil graphite [38], and modified fungus chaff biochar [52]. Interestingly, the obtained ZrO-SC sorbent showed a higher sorption capacity compared to the commercial activated carbon [106] (Table S4). Moreover, ZrO-SC also revealed a superior sorption capacity compared to the natural and modified clays, and zeolites [31,64,99] (Table S4). However, the q_{max} of ZrO-SC was relatively lower compared to clay nanotubes [4] (Table S4). Considering the high preparation cost of clay nanotubes compared to ZrO-SC suggested that the prepared ZrO-SC is a suitable and low-cost alternative adsorbent for eliminating pharmaceutical compounds, especially LVN from contaminated water.

3.4. The proposed adsorption mechanisms

Investigating the adsorption mechanism for any pollutant is essential, providing vital information about the properties and interaction of the adsorbent and adsorbed molecules under various environmental conditions. This information can then be used to develop effective treatments and technologies to reduce the toxic contaminants in the environment. In this study, considering the diverse functional constituents of SC and ZrO-SC, their high affinity towards LVN molecules can be remarkably explained by a series of different potential subsidiary synergistic scenarios (Fig. 8), as discussed below.

The influence of LVN molecules on the interlayer space of ZrO-SC was investigated by performing XRD analysis of ZrO-SC before and after LVN sorption (Fig. 8(a) and S2(a)). The characteristic smectite peak (d_{001}) of ZrO-SC before LVN sorption was found at 2 θ angle of 5.63° (interlayer spacing of 1.58 nm). Originally, the dimension of LVN molecule is 1.42 nm in length, 1.04 nm in height, and 0.66 nm in thickness (Fig. 8(b)) [100]. After LVN sorption, the intensity of the smectite peak decreased substantially and shifted towards a low 2 θ angle starting at 4.53° (1.96 nm). Expanding this peak (001) after LVN sorption ensured that the LVN molecules were positively inserted into ZrO-SC interlayer spaces (Fig. 8(a)). Also, the intensity of 001 peak was remarkably decreased. This can be attributed to the strong binding of LVN molecules with the hydroxyl groups of ZrO-SC. Similar observation with other pharmaceutical compounds was reported by other

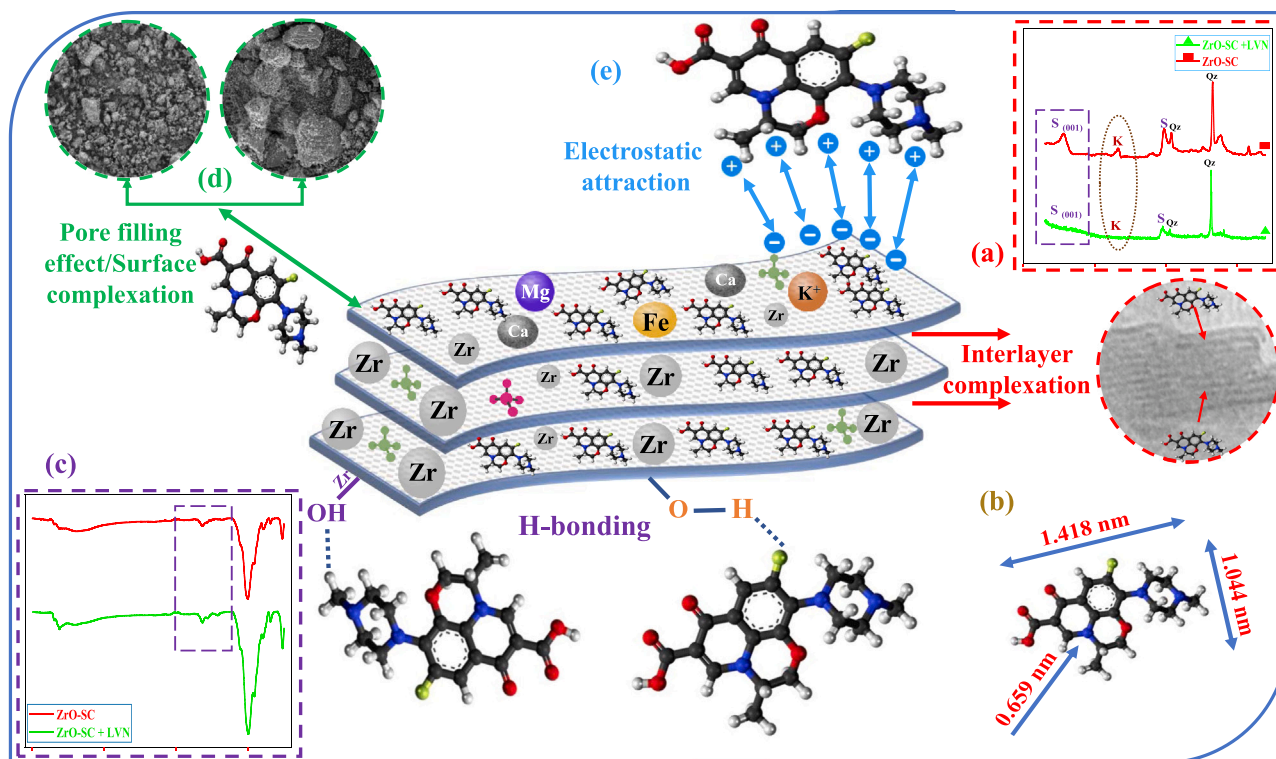


Fig. 8. The possible sorption mechanism of LVN onto ZrO-SC, (a) XRD analysis of ZrO-SC before and after LVN adsorption ($2\theta = 3\text{--}35^\circ$), (b) dimension of the LVN molecule, (c) FTIR spectra of ZrO-SC before and after LVN adsorption ($4000\text{--}400\text{ cm}^{-1}$), (d) SEM analysis of ZrO-SC before and after LVN adsorption, and (e) electrostatic attraction between ZrO-SC and LVN molecules.

researchers [94]. Moreover, the utilized SC sample contains a minor percentage of kaolinite mineral, evidenced by a peak at around $2\theta \approx 12.35^\circ$ (Fig. 8(a)). Comparing the spectra of ZrO-SC before and after LVN sorption showed a significant decrease in the intensity of the kaolinite characteristic peaks after LVN sorption (Fig. 8(a)). This observation indicates that kaolinite's crystal morphology is not obvious after LVN sorption. This phenomenon suggests that the minor kaolinite mineral in the ZrO-SC also contributed to the LVN sorption. Considering the low interlayer spaces of kaolinite ($\approx 0.72\text{ nm}$) and the relatively large dimensions of LVN molecule ($1.42 \times 1.04 \times 0.66\text{ nm}$) (Fig. 8(b)), suggested that H-bonds mainly dominated during the interactions between kaolinite structure and LVN molecules. Similar observations were reported regarding the intensity of the kaolinite peak after adsorption [61,89].

Similar procedure was conducted with ZrO-SC before and after LVN sorption via FT-IR analysis (Fig. 8(c) and S2(c)). Initially, the characteristic LVN bands appear within $1350\text{--}1600\text{ cm}^{-1}$ range [104]. On the other hand, ZrO-SC spectra are free from vibration bands between 3000 and 1300 cm^{-1} , except the band at 1635 cm^{-1} related to the bending vibration of water molecules. The existence of new bands in this range ($1350\text{--}1600\text{ cm}^{-1}$) after LVN sorption ((Fig. 8(c)) confirms that LVN molecules were successfully sorbed into ZrO-SC. The phenomena can be explained that the chemical complexation between the existing functional groups (O–H, Si–OH, and Al–OH) on ZrO-SC and LVN molecule involved the formation of hydrogen bonding between the siloxane groups or the basal oxygen of ZrO-SC sheets and the carboxylic acid groups of LVN [4,59]. Furthermore, the facile synthesis and incorporation of Zr into SC improved the capturing capacity of ZrO-SC as Zr ions can combine with silicon-oxygen tetrahedrons of SC in the occurrence of a stable [Si–O] and [HO–Zr] via H bonding. The corresponding Zr-modified SC binding groups (Zr–OH_2^+ and Zr–OH) had an admirable affinity towards LVN molecules through the exchange of (–OH^-) entities on the sorbent's surface and the successive creation of mononuclear monodentate and binuclear bidentate inner-sphere complexes [112].

Moreover, the SEM results for ZrO-SC after LVN sorption revealed that the ZrO-SC surface lost the roughness showing a stacky and spotted appearance (Fig. 8(d)). This phenomenon could also be credited to the fact that, after sorption, LVN molecules occupied the ZrO-SC surface pores. Considering the relatively high micropore diameter (13.19 nm) of ZrO-SC (Table 2) compared to the dimension of LVN molecule (Fig. 8(b)), raised the high possibility of the pore filling effect mechanism. Furthermore, the electrostatic attraction (Fig. 8(e)) could also occur between the ionized species of LVN (Section 3.3.1) and the charged binding sites of ZrO-SC surface, which induced the formation of the complexes under the effect of the Coulombic forces of the silicate layers [1].

3.5. Continuous fixed-bed column studies

The fixed-bed column experiments were performed, based on the optimum conditions from batch system, to assess the practical applicability of ZrO-SC compared to SC. The continuous fixed-bed column studies were conducted to scale up the process in addition to evaluate the behavior of the utilized adsorbents (SC and ZrO-SC) towards LVN removal. In this regard, three optimization parameters were studied, including inlet LVN (feeding adsorbate) concentration (mg L^{-1}), adsorbate flow rate (mL min^{-1}), and packed SC/ZrO-SC amount (mg) in the column. Furthermore, breakthrough curves of the studied parameters for all experimental runs were plotted (C_t/C_0 versus time) and illustrated in Fig. 9. Additionally, the experimental parameters of the experimental runs for SC and ZrO-SC are itemized and presented in Table 4.

3.5.1. Influence of SC/ZrO-SC loading

The packed adsorbent loading inside the column is also a quintessential parameter that influences the functioning of the continuous-flow mode and breakthrough curve. Fig. 9(a–b) illustrates the column performance towards LVN using two different SC/ZrO-SC loadings (50 and

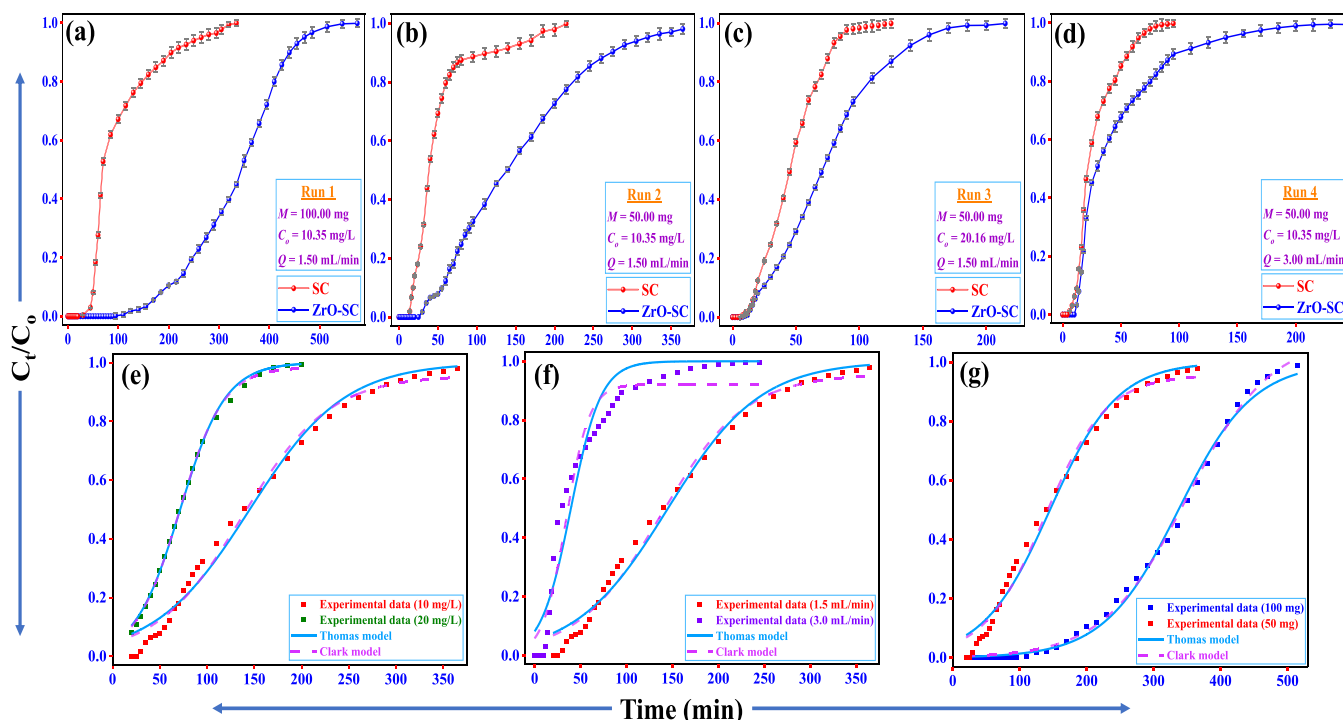


Fig. 9. Breakthrough curves of LVN adsorption onto SC and ZrO-SC at (a) Run 1, (b) Run 2, (c) Run 3, (d) Run 4, and (e, f, and g) the corresponding applied fixed-bed column kinetic models.

Table 4

The effect of flow rate, adsorbent loading and initial LVN concentration on the total adsorbed LVN (q_{total}), equilibrium uptake (q_{bed}), total removal efficiency of the column ($RE\%$) and total unadsorbed LVN concentration at equilibrium (C_{eq}) for SC and ZrO-SC sorbents.

Experiments	Run 1		Run 2		Run 3		Run 4	
Parameters	SC	ZrO-SC	SC	ZrO-SC	SC	ZrO-SC	SC	ZrO-SC
C_o (mg L ⁻¹)	10.35		10.35		20.16		10.35	
Q (mL min ⁻¹)	1.50		1.50		1.50		3.00	
M_{ZrO-SC} (mg)	100		50		50		50	
V_{eff} (mL)	502.5	1150.0	322.5	730.0	187.5	430.0	285.0	735.0
t_b (min)	30	95	13	40	5	12	4	10
t_{total} (min)	335	575	215	365	125	215	95	245
q_{total} (mg)	1.58	6.89	0.82	3.14	1.42	3.03	0.88	1.46
q_{bed} (mg g ⁻¹)	15.89	68.87	16.29	62.79	28.43	60.65	17.67	29.24
m_{total} (mg)	5.20	11.90	3.34	7.56	3.78	8.67	2.95	7.58
$RE(\%)$	30.57	57.86	24.42	41.55	27.60	34.98	29.95	19.29
C_{eq} (mg L ⁻¹)	7.19	4.36	7.83	6.05	12.58	13.11	7.25	8.32

100 mg). Plotting column data for SC and ZrO-SC using two sorbent loadings confirmed the superior performance of the synthesized ZrO-SC. The maximum bed capacity of ZrO-SC was 62.79 and 68.87 mg g⁻¹ for loading amounts of 50 and 100 mg, respectively, compared to 16.29 and 15.89 mg g⁻¹, for SC. This finding can be attributed to the enhanced specific surface area and interlayer spacing of ZrO-SC compared to SC. Thereafter, the optimum loading amount of the obtained ZrO-SC was assessed by comparing the performance of two different loading while keeping the other parameters constant. The obtained breakthrough curve and the calculated parameters confirmed that increasing the packed ZrO-SC loading (from 50 to 100 mg) significantly enhanced the column performance such as total operation time (from 365 to 575 min), $RE\%$ (from 41.55% to 57.86%), breakthrough time and steepness (from 40 to 95 min), and uptake capacity (from 62.79 to 68.87 mg g⁻¹) (Table 4). Additionally, the utilization of higher ZrO-SC loading (100 mg) effectively decreased the total LVN concentration (untreated) at equilibrium (C_{eq}) from 6.05 to 4.36 mg L⁻¹. Moreover, a corresponding noteworthy increase in the total effluent (treated) volume (V_{eff}) from 730.00 to 1150.00 mL was detected with increasing ZrO-SC

loading from 50 to 100 mg, respectively. Increasing ZrO-SC loading increases the bed height within the column, which extends the efficient interaction time between LVN molecules and ZrO-SC layers and surfaces. Consequently, an enhanced column performance was achieved, owing to the sufficient intraparticle diffusion rate and available binding sites [22].

3.5.2. Influence of inlet LVN concentration

The feeding concentration of the targeted pollutant into the column is a key factor that influences the functioning of a continuous flow adsorption system. Fig. 9(c) depicts the influence of the higher inlet LVN concentration (20.16 mg L⁻¹) on the breakthrough curves of SC and ZrO-SC.

The maximum bed capacity of ZrO-SC was 62.79 and 68.87 mg g⁻¹ for loading amounts of 50 and 100 mg, respectively, compared to 16.29 and 15.89 mg g⁻¹, for SC. This finding can be attributed to the enhanced specific surface area and interlayer spacing of ZrO-SC compared to SC. The two experimental runs (Run 2–3) revealed that increasing the inlet LVN concentration from 10.35 to 20.16 mg L⁻¹ adversely impacted

most column performance parameters (Fig. 9(b-c)). However, the total LVN concentrations (unadsorbed) at equilibrium (C_{eq}) and LVN delivered to the column system (m_{total}) were increased from 6.05 to 13.11 mg L⁻¹ and from 7.56 to 8.67 mg, respectively for ZrO-SC. Similar observation was also recorded for SC (Table 4). Specifically, the breakthrough time for ZrO-SC was shortened (12 min) compared to 40 min of the lower concentration (Table 4). Correspondingly, increasing initial LVN concentration adversely influenced the column RE% and total operational time (t_{total}), which decreased from 41.55% to 34.98% and 365–215 min, respectively (Table 4). On the contrary, the prolonged breakthrough curve was achieved with the lower LVN concentration owing to the targeted molecules' smoother transport (transport delayed effects) [24]. The remarked observations, such as decreased RE %, quick exhaustion times, and rapid breakthrough curves, could be attributed to the fast occupation rate of the accessible active binding sites of ZrO-SC with the inlet LVN concentration of 20.16 mg L⁻¹, resulting in a rapid saturation for the fixed-bed column. Other researchers also observed and reported similar trends [8,21].

3.5.3. Influence of inlet flow rate

Flow rate is also a significant parameter that highly impacts the adsorption performance in the continuous flow mode. The utilized flow rate in the column largely determines the direct contact time between the packed sorbent and adsorbate. Fig. 9(d) represents the column performance towards LVN using a flow rate of 3.00 mL min⁻¹, to assess its impact on column performance for SC and ZrO-SC (Run 4). The breakthrough curves generated based on the acquired data revealed a rapid onset of breakthrough with high flow rates for SC and ZrO-SC, in addition to a high residual concentration (7.25 and 8.32 mg L⁻¹, respectively) of LVN molecules in the effluent solution (Table 4). However, considering the high flow rate, ZrO-SC treated a total effluent volume of 735 mL compared to 285 mL for SC. These findings could be credited to inadequate interaction (residence) time between ZrO-SC and LVN, which consequently decreased the binding possibility between SC/ZrO-SC and LVN [56]. On the contrary, at the lower flow rate, the contact time between ZrO-SC and LVN molecules was maximized (Run 2), resulting in a higher RE% of 41.55% compared to 19.29% at a flow rate of 3.00 mL min⁻¹ (Table 4). Moreover, fast exhaustion time and steeper breakthrough curve were noticed with higher feeding LVN flow rate. This finding could be credited to high-rate and low-resistance mass transfer [5]. Accordingly, based on the plotted curve (Fig. 9(b)) and calculated parameters (Table 4), the inlet flow rate of 1.50 mL min⁻¹ exhibited a superior performance with LVN removal in the fixed-bed operation system.

Overall, the obtained data and the breakthrough curves from the four experimental runs revealed that the variation in the column conditions remarkably impacted the C_t/C_0 ratio in the following order: inlet flow rate > feeding (LVN) concentration > loading (bed height) amount. Furthermore, the optimum column conditions ($C_0 = 10.35$ mg L⁻¹, $M = 100.00$ mg, $Q = 1.50$ mL min⁻¹, (Run 1)) for ZrO-SC generated the highest q_{bed} and RE% of 68.87 mg g⁻¹ and 57.86%, respectively. However, the experimental runs recorded the lowest column efficiency with the other operational conditions ($C_0 = 10.35$ mg L⁻¹, $M = 50.00$ mg, $Q = 3.00$ mL min⁻¹, (Run 4)).

3.6. Fixed-bed kinetic modeling

Thomas and Clark models (non-linear forms) were employed to the obtained breakthrough curves of the investigated experimental runs for ZrO-SC (Fig. 9(e-g)). Table 5 demonstrates the calculated values of the fitted model parameters along with R^2 for the investigated experiments. Thomas model was originally proposed by Henry Thomas [88], on the assumptions of the pseudo-second-order kinetic and Langmuir isotherm models of batch mode adsorption system [40]. However, Clark model was initially proposed by Clark [17], on a combination aspect of the mass-transfer concept and Freundlich isotherm model. The obtained

Table 5

Parameters of Thomas and Clark models for LVN adsorption onto ZrO-SC via continuous flow system at different conditions.

<i>Thomas model</i>							
	C_0 (mg L ⁻¹)	Q (mL min ⁻¹)	K_{TH} (mL mg ⁻¹ min ⁻¹)	q_{exp} (mg g ⁻¹)	q_{TH} (mg g ⁻¹)	R^2	SSE
Run 1	10.35	1.50	0.151	68.87	68.64	0.996	0.004
Run 2	10.35	1.50	0.139	62.79	61.23	0.987	0.002
Run 3	20.16	1.50	0.068	60.65	59.60	0.998	0.001
Run 4	10.31	3.00	0.005	29.24	33.90	0.948	0.007
<i>Clark model</i>							
	C_0 (mg L ⁻¹)	Q (mL min ⁻¹)	M_{ZrO-SC} (mg)	A	r	R^2	SSE
Run 1	10.35	1.50	100	201.92	0.02	0.991	0.012
Run 2	10.35	1.50	50	130.46	0.03	0.988	0.102
Run 3	20.16	1.50	50	134.50	0.04	0.998	0.031
Run 4	10.31	3.00	50	196.41	0.08	0.956	0.046

data from the non-linear regression fitting of Thomas and Clark models at various experimental conditions confirmed that these models agreeably fit the obtained experimental data based on the high R^2 values (> 0.9) (Table 5). In the case of Thomas model, the theoretical q_{TH} was in line (close) with the experimental q_{exp} values for all experimental runs. Moreover, a negative correlation was observed, in which K_{TH} values decreased with increasing the inlet LVN concentrations and flow rate [21]. The model K_{TH} values refer to solute transfer rate from liquid to solid phase [23]. Therefore, the observed decrease in K_{TH} can be pointed out due to high driving force from mass transfer delivered to the column by increasing the abovementioned conditions. However, K_{TH} value was slightly increased with increasing ZrO-SC loading from 50 to 100 mg (Table 5). In the case of Clark model, with increasing the initial LVN concentration, the model constants (A and r) were increased. However, increasing ZrO-SC loading showed an elevation for the constant A and decrease in the constant r . Moreover, as the inlet flow rate increased, a significant rise in both values of A and r was noted (Table 5). These phenomena can be explained due to the dependency of this model on the Freundlich model in addition to the computability with low C_t/C_0 values [73,83]. A comparison of the applied models suggested that the Thomas model is the superior model to predict sorption of LVN molecules onto ZrO-SC via the continuous flow mode treatment process. Additionally, the good fitting of Clark model also indicates that LVN sorption occurred via a multi-layer process.

4. Cost estimation and economic evaluation

The cost estimation of any adsorbent used in water treatment depends on several factors, such as the employed method of activation, energy consumption cost, and the cost of used raw materials (including chemicals). Furthermore, the cost of the adsorbent can be impacted by its adsorption capacity, selectivity, operational expenditure, and rate of deterioration. Considering all these factors, an accurate estimate of the sorbent cost can be determined. In the current study, the average price of the utilized Egyptian SC is 0.031 €/kg (the international price ≈ 0.089 €/kg; referenced by US Geological Survey 2022). The energy consumption cost refers to the consumed energy through the synthesis phases of ZrO-SC. The energy cost per kilowatt-hour (KWh) was

calculated based on the average electricity rate in Finland for 2022 (0.05 €/KWh; halvinsäähkösopimus.fi). Consequently, the energy consumption cost can be calculated via Eq. (3) [34]. Therefore, the cost for LVN removal can be simply calculated based on the preparation costs of ZrO-SC, energy price, and the average adsorption capacity via Eq. (4) [39].

$$E_C = P_D \cdot L \cdot T \cdot C_C \quad (3)$$

$$\text{Adsorption cost} \left(\frac{\text{€}}{\text{g}_{\text{LVN}}} \right) = \frac{\left[\text{Material cost} \left(\frac{\text{€}}{\text{g}} \right) + E_C \left(\frac{\text{€(kW)}}{\text{g}} \right) \right]}{\text{Adsorption capacity} \cdot 10^{-3} \left(\frac{\text{g}}{\text{mg}} \right)} \quad (4)$$

where, E_C is the energy cost (€), P_D is the consumed power by each device (kW), L is the device factor load (0.5 for half-operation mode and 1.0 for full-operation mode). T is the operated time (h), and C_C is the energy price (€/KWh).

By applying the aforementioned equations, the calculations showed that the adsorption costs for SC and ZrO-SC are 0.0001 and 0.0021 €/g_{LVN}, respectively. Table 6 compares the sorption cost of the utilized sorbents as reported in the literature. The cost estimation of SC and ZrO-SC indicates that the prepared sorbent has favorable characteristics/cost relationship and can be applied in an actual wastewater treatment system. From the techno-economic point of view, SC can be effectively used with less polluted water, and ZrO-SC will be the best choice for highly contaminated water (i.e., hospitals and drug factories effluents). We believe that this approach will facilitate a successful treatment process at low-cost. Besides, the information gained from fixed-bed column studies confirms the synthesized sorbent's capability to scale up the treatment process. Finally, the outcomes of this study demonstrate that ZrO-SC can serve as a viable alternative to the costly adsorbents currently being employed.

5. Conclusions

A simple ion exchange-precipitation method was used to synthesize ZrO-SC hybrid composite adsorbent for the effective removal of LVN from water. The obtained ZrO-SC adsorbent was found to be stable under strong acidic solution (pH 1.0) and minimal loss of 0.3% of Zr was observed at pH 1.0. The experimental studies exhibited that 200 mg of $\text{ZrOCl}_2 \cdot 8 \text{H}_2\text{O}$ was the appropriate dosage to achieve the maximum sorption capacity of ZrO-SC towards LVN. The XRD and TEM results confirmed that the interlayer space of ZrO-SC was increased to 1.58 nm after the nano Zr impregnation, compared to 1.36 nm for SC. The obtained TG-DTA analysis indicated that SC impregnation by Zr particles significantly enhanced the thermal stability of ZrO-SC. The pH studies of LVN sorption confirmed that ZrO-SC has similar pH behavior as raw SC without any variation due to Zr modification. The Langmuir fitting showed a maximum uptake capacity of 356.98 mg g⁻¹ for ZrO-SC in the batch mode and the highest bed capacity of 68.87 mg g⁻¹ in the continuous flow mode. The mechanistic studies of LVN sorption onto ZrO-SC demonstrated the involvement of various sorption mechanisms, such as π - π interaction, non-stoichiometric cation exchange, electrostatic interaction, and pore filling. The spent ZrO-SC was effectively regenerated with acidic solution (0.2 M HCl) and displayed stable sorption for LVN over seven consecutive cycles, suggesting its potential and economic feasibility for the removal of LVN from contaminated water.

CRedit authorship contribution statement

Ali Maged: Conceptualization, Methodology, Investigation, Validation, Formal analysis, Writing – original draft. **Ahmed M. Elgarahy:** Investigation, Writing – review & editing. **Nils H. Haneklaus:** Writing – review & editing. **Ashok Kumar Gupta:** Writing – review & editing. **Pau-Loke Show:** Writing – review & editing. **Amit Bhatnagar:** Conceptualization, Supervision, Funding acquisition, Writing – review

Table 6

Comparison of the cost of removal of pollutants from water (g_{pollutant}) using various adsorbents.

Sorbent	Target pollutant	Sorption capacity (mg g ⁻¹)	Cost (€/g) ^a	References
Acid-modified kola nut husk	Ibuprofen	39.22	0.039	Bello et al. [14]
Coconut shell biochar	Basic red 09	10.00	0.650	Praveen et al. [78]
AC from Sugarcane Bagasse	Propane	≈ 0.36 mL _{VOC} g ⁻¹	0.0019	Pingolo et al. [32]
PVA/PEI electrospun nanofibers	Phosphorus	165.9	0.600	Li et al. [48]
Cherry kernels biochar	Pb(II)	94.48	0.039	Vukelic et al. [93]
Tomato seeds	Acid blue 92	36.23	0.110	Najafi et al. [69]
Rice husk biochar	Basic red 09	44.00	0.140	Praveen et al. [78]
Mesoporous silica	U(VI)	820.70	0.063	Sarafriz et al. [82]
Chitosan-calcite	Phosphorus	21.36	0.250	Pap et al. [75]
Pristine steel slag	Cu(II)	109.89	0.00003	Nikolić et al. [72]
Hierarchical ZnS-Ga ₂ S ₃	Cr(VI)	54.42	0.083	Qi et al. [80]
Green iron oxide nanoparticles (gINPs)	LVN	22.47	7.90	Altaf et al. [7]
SC	LVN	172.86	0.0001	Current work
ZrO-SC	LVN	356.98	0.0021	Current work

^a All costs are converted to Euro (€/€=1.08 “Jan 2023”)

& editing.

Declaration of Competing Interest

The authors declare that they have no known competing financial interests or personal relationships that could have appeared to influence the work reported in this paper.

Data Availability

Data will be made available on request.

Acknowledgments

Ali Maged expresses his sincere gratitude to the Cultural Affairs and Missions' sector, the Ministry of Higher Education, Arab Republic of Egypt, for his fully funded Postdoctoral fellowship grant (PD#82). Also, authors (Ali Maged and Nils H. Haneklaus) are thankful for the financial support toward this study by the Federal Ministry of Education, Science and Research (BMBWF) through Austria's Agency for Education and Internationalization (OeAD) [Grant Number: Africa UNINET P058]. Authors are thankful to the team of Flaticon.com for their creative icons used in the graphical abstract. Authors are thankful to Apurav Koyande, for his kind help in some characterization analyses. Authors also thank the Editor and all the anonymous reviewers for providing their insightful comments and suggestions to improve the quality of this work.

Appendix A. Supporting information

Supplementary data associated with this article can be found in the online version at doi:10.1016/j.jhazmat.2023.131325.

References

- [1] Abukhadra, M.R., Adli, A., El-Sherbeen, A.M., Ahmed Soliman, A.T., Abd Elgawad, A.E.E., 2020. Promoting the decontamination of different types of water pollutants (Cd²⁺, safranin dye, and phosphate) using a novel structure of exfoliated bentonite admixed with cellulose nanofiber. *J Environ Manag* 273, 111130. <https://doi.org/10.1016/j.jenvman.2020.111130>.
- [2] Abukhadra, M.R., AlHammadi, A.A., Seong Khim, J., Ajarem, J.S., Allam, A.A., 2022. Enhanced decontamination of Levofloxacin residuals from water using recycled glass based a green zinc oxide/mesoporous silica nanocomposite; adsorption and advanced oxidation studies. *J Clean Prod* 356, 131836. <https://doi.org/10.1016/j.jclepro.2022.131836>.
- [3] Abukhadra, M.R., Fathallah, W., El Kashief, F.A., El-Sherbeen, A.M., El-Meligy, M.A., Awwad, E.M., Luqman, M., 2021. Insight into the antimicrobial and photocatalytic properties of NiO impregnated MCM-48 for effective removal of pathogenic bacteria and toxic levofloxacin residuals. *Microporous Mesoporous Mater* 312, 110769. <https://doi.org/10.1016/j.micromeso.2020.110769>.
- [4] Abukhadra, M.R., Mohamed, A.S., El-Sherbeen, A.M., Soliman, A.T.A., 2020. Enhanced adsorption of toxic and biologically active levofloxacin residuals from wastewater using clay nanotubes as a novel fixed bed: column performance and optimization. *ACS Omega* 5, 26195–26205. <https://doi.org/10.1021/acsomega.0c03785>.
- [5] Ahmed, M.J., Hameed, B.H., 2018. Removal of emerging pharmaceutical contaminants by adsorption in a fixed-bed column: a review. *Ecotoxicol Environ Saf*. <https://doi.org/10.1016/j.ecoenv.2017.12.012>.
- [6] Al-Jabari, M.H., Sulaiman, S., Ali, S., Barakat, R., Mubarak, A., Khan, S.A., 2019. Adsorption study of levofloxacin on reusable magnetic nanoparticles: kinetics and antibacterial activity. *J Mol Liq* 291, 111249. <https://doi.org/10.1016/j.molliq.2019.111249>.
- [7] Altaf, S., Zafar, R., Zaman, W.Q., Ahmad, S., Yaqoob, K., Syed, A., Khan, A.J., Bilal, M., Arshad, M., 2021. Removal of levofloxacin from aqueous solution by green synthesized magnetite (Fe₃O₄) nanoparticles using Moringa oilfera: Kinetics and reaction mechanism analysis. *Ecotoxicol Environ Saf* 226, 112826. <https://doi.org/10.1016/j.ecoenv.2021.112826>.
- [8] Amador, I.C.B., Nunes, K.G.P., de Franco, M.A.E., Viegas, B.M., Macêdo, E.N., Fêris, L.A., Estumano, D.C., 2022. Application of approximate bayesian computational technique to characterize the breakthrough of paracetamol adsorption in fixed bed column. *Int Commun Heat Mass Transf* 132. <https://doi.org/10.1016/j.icheatmasstransfer.2022.105917>.
- [9] Andriani, L., Moreira Toja, R., Gauna, M.R., Conconi, M.S., Requejo, F.G., Rendtorff, N.M., 2017. Extended and local structural characterization of a natural and 800 °C fired Na-montmorillonite-Patagonian bentonite by XRD and Al/Si XANES. *Appl Clay Sci* 137, 233–240. <https://doi.org/10.1016/j.clay.2016.12.030>.
- [10] Antonelli, R., Malpass, G.R.P., Da Silva, M.G.C., Vieira, M.G.A., 2020. Adsorption of ciprofloxacin onto thermally modified bentonite clay: experimental design, characterization, and adsorbent regeneration. *J Environ Chem Eng* 8. <https://doi.org/10.1016/j.jece.2020.104553>.
- [11] Aryee, A.A., Han, R., 2022. A novel biocomposite based on peanut husk with antibacterial properties for the efficient sequestration of trimethoprim in solution: Batch and column adsorption studies. *Colloids Surf A Physicochem Eng Asp* 635, 128051. <https://doi.org/10.1016/j.colsurfa.2021.128051>.
- [12] Ayati, B., Newport, D., Wong, H., Cheeseman, C., 2022. Acid activated smectite clay as pozzolanic supplementary cementitious material. *Cem Concr Res* 162, 106969. <https://doi.org/10.1016/j.cemconres.2022.106969>.
- [13] Baldermann, A., Stamm, F.M., 2022. Effect of kinetics, pH, aqueous speciation and presence of ferrihydrite on vanadium (V) uptake by allophanic and smectitic clays. *Chem Geol* 607, 121022. <https://doi.org/10.1016/j.chemgeo.2022.121022>.
- [14] Bello, O.S., Alao, O.C., Alagbada, T.C., Agboola, O.S., Omotoba, O.T., Abikoye, O. R., 2021. A renewable, sustainable and low-cost adsorbent for ibuprofen removal. *Water Sci Technol* 83, 111–122. <https://doi.org/10.2166/wst.2020.551>.
- [15] Chaturvedi, G., Kaur, A., Umar, A., Khan, M.A., Algarni, H., Kansal, S.K., 2020. Removal of fluoroquinolone drug, levofloxacin, from aqueous phase over iron based MOFs, MIL-100(Fe). *J Solid State Chem* 281, 121029. <https://doi.org/10.1016/j.jssc.2019.121029>.
- [16] Chen, Z., Ma, W., Lu, G., Meng, F., Duan, S., Zhang, Z., Wei, L., Pan, Y., 2019. Adsorption of levofloxacin onto mechanochemistry treated zeolite: Modeling and site energy distribution analysis. *Sep Purif Technol* 222, 30–34. <https://doi.org/10.1016/j.seppur.2019.04.010>.
- [17] Clark, R.M., 1987. Evaluating the cost and performance of field-scale granular activated carbon systems. *Environ Sci Technol* 21, 573–580. <https://doi.org/10.1021/es00160a008>.
- [18] Costigan, E.M., Oehler, M.A., MacRae, J.D., 2022. Phosphorus recovery from recirculating aquaculture systems: adsorption kinetics and mechanism. *J Water Process Eng* 49, 102992. <https://doi.org/10.1016/j.jwpe.2022.102992>.
- [19] Cristóvão, M.B., Tela, S., Silva, A.F., Oliveira, M., Bento-Silva, A., Bronze, M.R., Crespo, M.T.B., Crespo, J.G., Nunes, M., Pereira, V.J., 2021. Occurrence of antibiotics, antibiotic resistance genes and viral genomes in wastewater effluents and their treatment by a pilot scale nanofiltration unit. *Membr (Basel)* 11, 1–16. <https://doi.org/10.3390/membranes11010009>.
- [20] Darweesh, T.M., Ahmed, M.J., 2017. Batch and fixed bed adsorption of levofloxacin on granular activated carbon from date (*Phoenix dactylifera* L.) stones by KOH chemical activation. *Environ Toxicol Pharmacol* 50, 159–166. <https://doi.org/10.1016/j.etap.2017.02.005>.
- [21] Das, L., Sengupta, S., Das, P., Bhowal, A., Bhattacharjee, C., 2021. Experimental and numerical modeling on dye adsorption using pyrolyzed mesoporous biochar in batch and fixed-bed column reactor: isotherm, thermodynamics, mass transfer, kinetic analysis. *Surf Interfaces* 23, 100985. <https://doi.org/10.1016/j.surf.2021.100985>.
- [22] De Sá, I.C., De Oliveira, P.M., Nossol, E., Borges, P.H.S., Lepri, F.G., Semaan, F.S., Dornellas, R.M., Pacheco, W.F., 2022. Modified dry bean pod waste (*Phaseolus vulgaris*) as a biosorbent for fluorescein removal from aqueous media: batch and fixed bed studies. *J Hazard Mater* 424. <https://doi.org/10.1016/j.jhazmat.2021.127723>.
- [23] Dovi, E., Aryee, A.A., Kani, A.N., Mpatani, F.M., Li, J., Li, Z., Qu, L., Han, R., 2021. Functionalization of walnut shell by grafting amine groups to enhance the adsorption of Congo red from water in batch and fixed-bed column modes. *J Environ Chem Eng* 9. <https://doi.org/10.1016/j.jece.2021.106301>.
- [24] Dovi, E., Aryee, A.A., Kani, A.N., Mpatani, F.M., Li, J., Qu, L., Han, R., 2022. High-capacity amino-functionalized walnut shell for efficient removal of toxic hexavalent chromium ions in batch and column mode. *J Environ Chem Eng* 10. <https://doi.org/10.1016/j.jece.2022.107292>.
- [25] El-Maraghy, C.M., El-Borady, O.M., El-Naem, O.A., 2020. Effective removal of levofloxacin from pharmaceutical wastewater using synthesized zinc oxid, graphen oxid nanoparticles compared with their combination. *Sci Rep* 10, 1–13. <https://doi.org/10.1038/s41598-020-61742-4>.
- [26] Elgaray, A.M., Elwakeel, K.Z., Mohammad, S.H., Elshoubaky, G.A., 2021. A critical review of biosorption of dyes, heavy metals and metalloids from wastewater as an efficient and green process. *Clean Eng Technol*. <https://doi.org/10.1016/j.clet.2021.100209>.
- [27] Elgaray, A.M., Elwakeel, K.Z., Mohammad, S.H., Elshoubaky, G.A., 2020. Multifunctional eco-friendly sorbent based on marine brown algae and bivalve shells for subsequent uptake of Congo red dye and copper(II) ions. *J Environ Chem Eng* 8. <https://doi.org/10.1016/j.jece.2020.103915>.
- [28] Elgaray, A.M., Maged, A., Elwakeel, K.Z., El-Gohary, F., El-Qelish, M., 2023. Tuning cationic/anionic dyes sorption from aqueous solution onto green algal biomass for biohydrogen production. *Environ Res* 216, 114522. <https://doi.org/10.1016/j.envres.2022.114522>.
- [29] Ewis, D., Ba-Abbad, M.M., Benamor, A., El-Naas, M.H., 2022. Adsorption of organic water pollutants by clays and clay minerals composites: a comprehensive review. *Appl Clay Sci* 229, 106686. <https://doi.org/10.1016/j.clay.2022.106686>.
- [30] Fan, G., Yang, S., Du, B., Luo, J., Lin, X., Li, X., 2022. Sono-photo hybrid process for the synergistic degradation of levofloxacin by FeVO₄/BiVO₄: mechanisms and kinetics. *Environ Res* 204, 112032. <https://doi.org/10.1016/j.envres.2021.112032>.
- [31] Farajfaed, S., Sharifian, S., Asasian-Kolur, N., Sillanpää, M., 2021. Granular silica pillared clay for levofloxacin and gemifloxacin adsorption from aqueous systems. *J Environ Chem Eng* 9, 106306. <https://doi.org/10.1016/j.jece.2021.106306>.
- [32] Fingolo, A.C., Klein, B.C., Rezende, M.C.A.F., Silva e Souza, C.A., Yuan, J., Yin, G., Bonomi, A., Martinez, D.S.T., Strauss, M., 2020. Techno-economic assessment and critical properties tuning of activated carbons from pyrolyzed sugarcane bagasse. *Waste Biomass-Valoriz* 11, 1–13. <https://doi.org/10.1007/s12649-019-00774-y>.
- [33] Funes, I.G.A., Peralta, M.E., Pettinari, G.R., Carlos, L., Parolo, M.E., 2020. Facile modification of montmorillonite by intercalation and grafting: the study of the binding mechanisms of a quaternary alkylammonium surfactant. *Appl Clay Sci* 195, 105738. <https://doi.org/10.1016/j.clay.2020.105738>.
- [34] Gkika, D., Liakos, E.V., Vordos, N., Kontogoulidou, C., Magafas, L., Bikiaris, D.N., Bandekas, D.V., Mitropoulos, A.C., Kyzas, G.Z., 2019. Cost estimation of polymeric adsorbents. *Polym (Basel)* 11. <https://doi.org/10.3390/polym11050925>.
- [35] Hasanvandian, F., Shokri, A., Moradi, M., Kakavandi, B., Rahman Setayesh, S., 2022. Encapsulation of spinel CuCo₂O₄ hollow sphere in V₂O₅-decorated graphitic carbon nitride as high-efficiency double Z-type nanocomposite for levofloxacin photodegradation. *J Hazard Mater* 423, 127090. <https://doi.org/10.1016/j.jhazmat.2021.127090>.
- [36] Hu, Z., Ge, M., Guo, C., 2021. Efficient removal of levofloxacin from different water matrices via simultaneous adsorption and photocatalysis using a magnetic Ag₃PO₄/rGO/CoFe₂O₄ catalyst. *Chemosphere* 268, 128834. <https://doi.org/10.1016/j.chemosphere.2020.128834>.
- [37] Huang, W.Y., Li, D., Liu, Z.Q., Tao, Q., Zhu, Y., Yang, J., Zhang, Y.M., 2014. Kinetics, isotherm, thermodynamic, and adsorption mechanism studies of La(OH) 3-modified exfoliated vermiculites as highly efficient phosphate adsorbents. *Chem Eng J* 236, 191–201. <https://doi.org/10.1016/j.cej.2013.09.077>.
- [38] Idrees, A.S., Sulaiman, S.M., Al-Jabari, M.H., Nazal, M.K., Mubarak, A.M., N. Al-Rimawi, L., 2022. Pencil graphite supported nano zero-valent iron for removal of levofloxacin from aqueous solution: Effects of pH, kinetic and biological activity. *Arab J Chem* 15, 104309. <https://doi.org/10.1016/j.arabjc.2022.104309>.
- [39] Ighalo, J.O., Omoarukhe, F.O., Ojukwu, V.E., Iwuozor, K.O., Igwegbe, C.A., 2022. Cost of adsorbent preparation and usage in wastewater treatment: a review. *Clean Chem Eng* 3, 100042. <https://doi.org/10.1016/j.clce.2022.100042>.
- [40] Iheanacho, O.C., Nwabanne, J.T., Obi, C.C., Onu, C.E., 2021. Packed bed column adsorption of phenol onto corn cob activated carbon: linear and nonlinear kinetics modeling. *South Afr J Chem Eng* 36, 80–93. <https://doi.org/10.1016/j.sajce.2021.02.003>.
- [41] Jia, A., Zhao, Y., Liu, Z., Zhang, F., Shi, C., Liu, Z., Hong, M., Li, Y., 2023. New insight into enhanced transport of multi-component porous covalent-organic polymers with alkyl chains as injection agents for levofloxacin removal in saturated sand columns. *Sci Total Environ* 862. <https://doi.org/10.1016/j.scitotenv.2022.160773>.

- [42] Kalantari, K., Ahmad, M.B., Fard Masoumi, H.R., Shamel, K., Basri, M., Khandanlou, R., 2015. Rapid and high capacity adsorption of heavy metals by Fe3O4/montmorillonite nanocomposite using response surface methodology: preparation, characterization, optimization, equilibrium isotherms, and adsorption kinetics study. *J Taiwan Inst Chem Eng* 49, 192–198. <https://doi.org/10.1016/j.jtice.2014.10.025>.
- [43] Keikha, M., Askari, P., Ghazvini, K., Karbalaee, M., 2022. Levofloxacin-based therapy as an efficient alternative for eradicating *Helicobacter pylori* infection in Iran: a systematic review and meta-analysis. *J Glob Antimicrob Resist* 29, 420–429. <https://doi.org/10.1016/j.jgar.2021.10.019>.
- [44] Kumararaja, P., Manjaiah, K.M., Datta, S.C., Sarkar, B., 2017. Remediation of metal contaminated soil by aluminium pillared bentonite: synthesis, characterisation, equilibrium study and plant growth experiment. *Appl Clay Sci* 137, 115–122. <https://doi.org/10.1016/J.CLAY.2016.12.017>.
- [45] Lemos, B.R.S., Soares, A.R., Teixeira, A.P.C., Ardisson, J.D., Fernandez-Outon, L. E., Amorim, C.C., Lago, R.M., Moura, F.C.C., 2016. Growth of carbon structures on chrysotile surface for organic contaminants removal from wastewater. *Chemosphere* 159, 602–609. <https://doi.org/10.1016/j.chemosphere.2016.06.022>.
- [46] Li, H., Shan, C., Zhang, Y., Cai, J., Zhang, W., Pan, B., 2016. Arsenate adsorption by hydrous ferric oxide nanoparticles embedded in cross-linked anion exchanger: effect of the host pore structure. *ACS Appl Mater Interfaces* 8, 3012–3020. <https://doi.org/10.1021/acsmi.5b09832>.
- [47] Li, M., Zhang, B., Zou, S., Liu, Q., Yang, M., 2020. Highly selective adsorption of vanadium (V) by nano-hydrous zirconium oxide-modified anion exchange resin. *J Hazard Mater* 384, 121386. <https://doi.org/10.1016/j.jhazmat.2019.121386>.
- [48] Li, S., Huang, X., Liu, J., Lu, L., Peng, K., Bhattarai, R., 2020. PVA/PEI crosslinked electropositive nanofibers with embedded La(OH)3 nanorod for selective adsorption of high flux low concentration phosphorus. *J Hazard Mater* 384, 121457. <https://doi.org/10.1016/j.jhazmat.2019.121457>.
- [49] Liu, D., Deng, S., Maimaiti, A., Wang, B., Huang, J., Wang, Y., Yu, G., 2018. As (III) and As(V) adsorption on nanocomposite of hydrated zirconium oxide coated carbon nanotubes. *J Colloid Interface Sci* 511, 277–284. <https://doi.org/10.1016/j.jcis.2017.10.004>.
- [50] Liu, D., Deng, S., Vakili, M., Du, R., Tao, L., Sun, J., Wang, B., Huang, J., Wang, Y., Yu, G., 2019. Fast and high adsorption of Ni(II) on vermiculite-based nanoscale hydrated zirconium oxides. *Chem Eng J* 360, 1150–1157. <https://doi.org/10.1016/j.cej.2018.10.178>.
- [51] Liu, Y., Dong, C., Wei, H., Yuan, W., Li, K., 2015. Adsorption of levofloxacin onto an iron-pillared montmorillonite (clay mineral): Kinetics, equilibrium and mechanism. *Appl Clay Sci* 118, 301–307. <https://doi.org/10.1016/j.clay.2015.10.010>.
- [52] Luo, T., Wu, L., Jia, B., Zeng, Y., Hao, J., He, S., Liang, L., 2023. Research on adsorption mechanisms of levofloxacin over fungus chaff biochar modified by combination of alkali activation and copper-cobalt metallic oxides. *Biomass–Converters Biorefinery* 1–15. <https://doi.org/10.1007/s13399-023-03803-y>.
- [53] Luo, X., Wang, C., Wang, L., Deng, F., Luo, S., Tu, X., Au, C., 2013. Nanocomposites of graphene oxide-hydrated zirconium oxide for simultaneous removal of As(III) and As(V) from water. *Chem Eng J* 220, 98–106. <https://doi.org/10.1016/j.cej.2013.01.017>.
- [54] Lyu, J., Ge, M., Hu, Z., Guo, C., 2020. One-pot synthesis of magnetic CuO/Fe2O3/CuFe2O4 nanocomposite to activate persulfate for levofloxacin removal: Investigation of efficiency, mechanism and degradation route. *Chem Eng J* 389, 124456. <https://doi.org/10.1016/j.cej.2020.124456>.
- [55] Maged, A., Abu El-Magd, S.A., Radwan, A.E., Kharbush, S., Zamzam, S., 2023. Evaluation insight into Abu Zenima clay deposits as a prospective raw material source for ceramics industry: remote sensing and characterization. *Sci Rep* 13, 1–16. <https://doi.org/10.1038/s41598-022-26484-5>.
- [56] Maged, A., Dissanayake, P.D., Yang, X., Pathirannahalage, C., Bhatnagar, A., Ok, Y.S., 2021. New mechanistic insight into rapid adsorption of pharmaceuticals from water utilizing activated biochar. *Environ Res* 202, 111693. <https://doi.org/10.1016/j.envres.2021.111693>.
- [57] Maged, A., Iqbal, J., Kharbush, S., Ismael, I.S.I.S., Bhatnagar, A., 2020. Tuning tetracycline removal from aqueous solution onto activated 2:1 layered clay mineral: Characterization, sorption and mechanistic studies. *J Hazard Mater* 384, 121320. <https://doi.org/10.1016/j.jhazmat.2019.121320>.
- [58] Maged, A., Ismael, I.S., Kharbush, S., Sarkar, B., Peräniemi, S., Bhatnagar, A., 2020. Enhanced interlayer trapping of Pb(II) ions within kaolinite layers: intercalation, characterization, and sorption studies. *Environ Sci Pollut Res* 27, 1870–1887. <https://doi.org/10.1007/s11356-019-06845-w>.
- [59] Maged, A., Kharbush, S., Ismael, I.S.I.S., Bhatnagar, A., 2020. Characterization of activated bentonite clay mineral and the mechanisms underlying its sorption for ciprofloxacin from aqueous solution. *Environ Sci Pollut Res* 27, 1–18. <https://doi.org/10.1007/s11356-020-09267-1>.
- [60] Mahmoud, M.E., El-Ghanam, A.M., Mohamed, R.H.A., Saad, S.R., 2020. Enhanced adsorption of Levofloxacin and Ceftriaxone antibiotics from water by assembled composite of nanotitanium oxide/chitosan/nano-bentonite. *Mater Sci Eng C* 108, 110199. <https://doi.org/10.1016/j.msec.2019.110199>.
- [61] Mao, X., Liu, H., Chu, Z., Chen, T., Zou, X., Chen, D., Zhang, X., Hu, J., 2022. Adsorption of lead by kaolinite, montmorillonite, goethite and ferrihydrite: performance and mechanisms based on quantitative analysis. *Clay Min* 1–11. <https://doi.org/10.1180/clm.2022.41>.
- [62] Martínez-Alcalá, I., Pellicer-Martínez, F., Fernández-López, C., 2018. Pharmaceutical grey water footprint: accounting, influence of wastewater treatment plants and implications of the reuse. *Water Res* 135, 278–287. <https://doi.org/10.1016/j.watres.2018.02.033>.
- [63] Martínez, J.M., Conconi, M.S., Booth, F., Rendtorff, N.M., 2021. High-temperature transformations of Zr-pillared bentonite. *J Therm Anal Calor* 145, 51–58. <https://doi.org/10.1007/S10973-020-09681-0/TABLES/4>.
- [64] Martucci, A., Pasti, L., Marchetti, N., Cavazzini, A., Dondi, F., Alberti, A., 2012. Adsorption of pharmaceuticals from aqueous solutions on synthetic zeolites. *Microporous Mesoporous Mater* 148, 174–183. <https://doi.org/10.1016/j.micromeso.2011.07.009>.
- [65] Matangou, B., Dedzo, G.K., Dzene, L., Nanseu-Njiki, C.P., Ngamei, E., 2021. Encapsulation of butylimidazole in smectite and slow release for enhanced copper corrosion inhibition. *Appl Clay Sci* 213, 106266. <https://doi.org/10.1016/j.clay.2021.106266>.
- [66] Mishra, A., Mehta, A., Sharma, M., Basu, S., 2017. Enhanced heterogeneous photodegradation of VOC and dye using microwave synthesized TiO2/Clay nanocomposites: A comparison study of different type of clays. *J Alloy Compd* 694, 574–580. <https://doi.org/10.1016/j.jallcom.2016.10.036>.
- [67] Mpelane, S., Mketo, N., Bingwa, N., Nomngongo, P.N., 2022. Synthesis of mesoporous iron oxide nanoparticles for adsorptive removal of levofloxacin from aqueous solutions: Kinetics, isotherms, thermodynamics and mechanism. *Alex Eng J* 61, 8457–8468. <https://doi.org/10.1016/j.aej.2022.02.014>.
- [68] Mpelane, S., Mketo, N., Mlambo, M., Bingwa, N., Nomngongo, P.N., 2022. One-step synthesis of a Mn-doped Fe2O3/GO core-shell nanocomposite and its application for the adsorption of levofloxacin in aqueous solution. *ACS Omega* 7, 23302–23314. <https://doi.org/10.1021/acsomega.2c01460>.
- [69] Najafi, H., Pajootan, E., Ebrahimi, A., Arami, M., 2016. The potential application of tomato seeds as low-cost industrial waste in the adsorption of organic dye molecules from colored effluents. *Desalin Water Treat* 57, 15026–15036. <https://doi.org/10.1080/19443994.2015.1072060>.
- [70] Nakarmi, K.J., Daneshvar, E., Eshaq, G., Puro, L., Maiti, A., Nidheesh, P.V., Wang, H., Bhatnagar, A., 2022. Synthesis of biochar from iron-free and iron-containing microalgal biomass for the removal of pharmaceuticals from water. *Environ Res* 214, 114041. <https://doi.org/10.1016/j.envres.2022.114041>.
- [71] Nashtifan, S.G., Azadmehr, A., Maghsoudi, A., 2017. Comparative and competitive adsorptive removal of Ni2+ and Cu2+ from aqueous solution using iron oxide-vermiculite composite. *Appl Clay Sci* 140, 38–49. <https://doi.org/10.1016/j.clay.2016.12.020>.
- [72] Nikolić, I., Durović, D., Tadić, M., Radmilović, V.V., Radmilović, V.R., 2020. Adsorption kinetics, equilibrium, and thermodynamics of Cu2+ on pristine and alkali activated steel slag. *Chem Eng Commun* 207, 1278–1297. <https://doi.org/10.1080/00986445.2019.1685986>.
- [73] Ostaszewski, P., Długosz, O., Banach, M., 2022. Analysis of measuring methods of the concentration of methylene blue in the sorption process in fixed-bed column. *Int J Environ Sci Technol* 19, 1–8. <https://doi.org/10.1007/s13762-021-03156-x>.
- [74] Panna, W., Szumera, M., Wyszomirski, P., 2016. The impact of modifications of the smectite-bearing raw materials on their thermal expansion ability. *J Therm Anal Calorim* 123, 1153–1161. <https://doi.org/10.1007/s10973-015-5023-0>.
- [75] Pap, S., Kirk, C., Bremner, B., Turk Sekulic, M., Shearer, L., Gibb, S.W., Taggart, M.A., 2020. Low-cost chitosan-calcite adsorbent development for potential phosphate removal and recovery from wastewater effluent. *Water Res* 173, 115573. <https://doi.org/10.1016/j.watres.2020.115573>.
- [76] Peng, J., He, Y.Y., Zhang, Z.Y., Chen, X.Z., Jiang, Y.L., Guo, H., Yuan, J.P., Wang, J.H., 2022. Removal of levofloxacin by an oleaginous microalgae *Chromocloris zofigiensis* in the heterotrophic mode of cultivation: Removal performance and mechanism. *J Hazard Mater* 425, 128036. <https://doi.org/10.1016/j.jhazmat.2021.128036>.
- [77] Peng, Y., Azeem, M., Li, R., Xing, L., Li, Y., Zhang, Y., Guo, Z., Wang, Q., Ngo, H. H., Qu, G., Zhang, Z., 2022. Zirconium hydroxide nanoparticle encapsulated magnetic biochar composite derived from rice residue: application for As(III) and As(V) polluted water purification. *J Hazard Mater* 423, 127081. <https://doi.org/10.1016/j.jhazmat.2021.127081>.
- [78] Praveen, S., Gokulan, R., Pushpa, T.B., Jegan, J., 2021. Techno-economic feasibility of biochar as biosorbent for basic dye sequestration. *J Indian Chem Soc* 98, 100107. <https://doi.org/10.1016/j.jcis.2021.100107>.
- [79] Purceno, A.D., Barrioni, B.R., Dias, A., da Costa, G.M., Lago, R.M., Moura, F.C.C., 2011. Carbon nanostructures-modified expanded vermiculites produced by chemical vapor deposition from ethanol. *Appl Clay Sci* 54, 15–19. <https://doi.org/10.1016/j.clay.2011.06.012>.
- [80] Qi, Y., Fan, Y., Liu, T., Zheng, X., 2020. Flower-like hierarchical ZnS-Ga2S3 heterojunction for the adsorption-photo-reduction of Cr(VI). *Chemosphere* 261, 127824. <https://doi.org/10.1016/j.chemosphere.2020.127824>.
- [81] Rehman, M.U., Manan, A., Uzair, M., Khan, A.S., Ullah, A., Ahmad, A.S., Wazir, A. H., Qazi, I., Khan, M.A., 2021. Physicochemical characterization of Pakistani clay for adsorption of methylene blue: kinetic, isotherm and thermodynamic study. *Mater Chem Phys* 269, 124722. <https://doi.org/10.1016/j.matchemphys.2021.124722>.
- [82] Sarafraz, H., Alahyarizadeh, G., Minucmehr, A., Modaberi, H., Naserbegi, A., 2019. Economic and efficient phosphonic functional groups mesoporous silica for uranium selective adsorption from aqueous solutions. *Sci Rep* 9, 1–10. <https://doi.org/10.1038/s41598-019-46090-2>.
- [83] Song, J., Zou, W., Bian, Y., Su, F., Han, R., 2011. Adsorption characteristics of methylene blue by peanut husk in batch and column modes. *Desalination* 265, 119–125. <https://doi.org/10.1016/j.desal.2010.07.041>.
- [84] Steudel, A., Batenburg, L.F.F., Fischer, H.R.R., Weidler, P.G.G., Emmerich, K., 2009. Alteration of swelling clay minerals by acid activation. *Appl Clay Sci* 44, 105–115. <https://doi.org/10.1016/J.CLAY.2009.02.002>.
- [85] Sulaiman, S.M., Al-Jabari, M.H., 2021. Enhanced adsorptive removal of diclofenac sodium from aqueous solution by bentonite-supported nanoscale zero-

- valent iron. Arab J Basic Appl Sci 28, 51–63. <https://doi.org/10.1080/25765299.2021.1878655>.
- [86] Tang, X., Fan, W., Zhang, S., Yan, B., Zheng, H., 2023. The improvement of levofloxacin and tetracycline removal from simulated water by thermosensitive flocculant: Mechanisms and simulation. Sep Purif Technol 309, 123027. <https://doi.org/10.1016/j.seppur.2022.123027>.
- [87] Tao, J., Yang, J., Ma, C., Li, J., Du, K., Wei, Z., Chen, C., Wang, Z., Zhao, C., Deng, X., 2020. Cellulose nanocrystals/graphene oxide composite for the adsorption and removal of levofloxacin hydrochloride antibiotic from aqueous solution: nanocomposites adsorb antibiotics. R Soc Open Sci 7. <https://doi.org/10.1098/rsos.200857>.
- [88] Thomas, H.C., 1944. Heterogeneous ion exchange in a flowing system. J Am Chem Soc 66, 1664–1666. <https://doi.org/10.1021/ja01238a017>.
- [89] Tian, L., Fu, K., bin, Chen, S., Yao, J., Bian, L., 2022. Comparison of microscopic adsorption characteristics of Zn(II), Pb(II), and Cu(II) on kaolinite. Sci Rep 12, 1–13. <https://doi.org/10.1038/s41598-022-20238-z>.
- [90] Trindade, M.J., Dias, M.I., Corrado, J., Rocha, F., 2009. Mineralogical transformations of calcareous rich clays with firing: a comparative study between calcite and dolomite rich clays from Algarve, Portugal. Appl Clay Sci 42, 345–355. <https://doi.org/10.1016/j.clay.2008.02.008>.
- [91] Tzabar, N., ter Brake, H.J.M., 2016. Adsorption isotherms and Sips models of nitrogen, methane, ethane, and propane on commercial activated carbons and polyvinylidene chloride. Adsorption 22, 901–914. <https://doi.org/10.1007/s10450-016-9794-9>.
- [92] Ullah, A., Zahoor, M., Alam, S., Ullah, R., Alqahtani, A.S., Mahmood, H.M., 2019. Separation of levofloxacin from industry effluents using novel magnetic nanocomposite and membranes hybrid processes. Biomed Res Int 2019. <https://doi.org/10.1155/2019/5276841>.
- [93] Vukelic, D., Boskovic, N., Agarski, B., Radonic, J., Budak, I., Pap, S., Turk Sekulic, M., 2018. Eco-design of a low-cost adsorbent produced from waste cherry kernels. J Clean Prod 174, 1620–1628. <https://doi.org/10.1016/j.jclepro.2017.11.098>.
- [94] Wang, C.J., Li, Z., Jiang, W.T., Jean, J.S., Liu, C.C., 2010. Cation exchange interaction between antibiotic ciprofloxacin and montmorillonite. J Hazard Mater 183, 309–314. <https://doi.org/10.1016/j.jhazmat.2010.07.025>.
- [95] Wang, G., Cheng, H., 2023. Facile synthesis of a novel recyclable dual Z-scheme WO₃/NiFe₂O₄/BiOBr composite with broad-spectrum response and enhanced sonocatalytic performance for levofloxacin removal in aqueous solution. Chem Eng J 461, 141941. <https://doi.org/10.1016/j.cej.2023.141941>.
- [96] Wang, J., Chu, L., Wojnárovits, L., Takács, E., 2020. Occurrence and fate of antibiotics, antibiotic resistant genes (ARGs) and antibiotic resistant bacteria (ARB) in municipal wastewater treatment plant: An overview. Sci Total Environ. <https://doi.org/10.1016/j.scitotenv.2020.140997>.
- [97] Wang, Z., Chen, Y., Wang, L., Zheng, J., Fan, Y., Zhang, S., 2023. Rapid and efficient removal of toxic ions from water using Zr-based MOFs@PIM hierarchical porous nanofibre membranes. Chem Eng J 452, 139198. <https://doi.org/10.1016/j.cej.2022.139198>.
- [98] Wang, Z., Jang, H.M., 2022. Comparative study on characteristics and mechanism of levofloxacin adsorption on swine manure biochar. Bioresour Technol 351, 127025. <https://doi.org/10.1016/j.biortech.2022.127025>.
- [99] Wei, M., Lv, D., Cao, L.H., Zhou, K., Jiang, K., 2021. Adsorption behaviours and transfer simulation of levofloxacin in silty clay. Environ Sci Pollut Res 28, 46291–46302. <https://doi.org/10.1007/s11356-021-13955-x>.
- [100] Wei, N., Jia, L., Shang, Z., Gong, J., Wu, S., Wang, J., Tang, W., 2019. Polymorphism of levofloxacin: structure, properties and phase transformation. CrystEngComm 21, 6196–6207. <https://doi.org/10.1039/c9ce00847k>.
- [101] Worch, E., 2021. Adsorption technology in water treatment: fundamentals, processes, and modeling. Adsorpt Technol Water Treat: Fundam, Process, Model. <https://doi.org/10.1515/9783110240238>.
- [102] Wu, X., Liu, P., Huang, H., Gao, S., 2020. Adsorption of triclosan onto different aged polypropylene microplastics: Critical effect of cations. Sci Total Environ 717, 137033. <https://doi.org/10.1016/j.scitotenv.2020.137033>.
- [103] Xiang, Y., Xu, Z., Zhou, Y., Wei, Y., Long, X., He, Y., Zhi, D., Yang, J., Luo, L., 2019. A sustainable ferromanganese biochar adsorbent for effective levofloxacin removal from aqueous medium. Chemosphere 237, 124464. <https://doi.org/10.1016/j.chemosphere.2019.124464>.
- [104] Xiong, Q., Liu, Y.S., Hu, L.X., Shi, Z.Q., Ying, G.G., 2020. Levofloxacin and sulfamethoxazole induced alterations of biomolecules in Pseudokirchneriella subcapitata. Chemosphere 253, 126722. <https://doi.org/10.1016/j.chemosphere.2020.126722>.
- [105] Xu, Z., Xiang, Y., Zhou, H., Yang, J., He, Y., Zhu, Z., Zhou, Y., 2021. Manganese ferrite modified biochar from vinasse for enhanced adsorption of levofloxacin: Effects and mechanisms. Environ Pollut 272, 115968. <https://doi.org/10.1016/j.envpol.2020.115968>.
- [106] Yang, D., Li, J., Luo, L., Deng, R., He, Q., Chen, Y., 2020. Exceptional levofloxacin removal using biochar-derived porous carbon sheets: mechanisms and density-functional-theory calculation. Chem Eng J 387, 124103. <https://doi.org/10.1016/j.cej.2020.124103>.
- [107] Yao, B., Luo, Z., Du, S., Yang, J., Zhi, D., Zhou, Y., 2021. Sustainable biochar/MgFe₂O₄ adsorbent for levofloxacin removal: adsorption performances and mechanisms. Bioresour Technol 340. <https://doi.org/10.1016/j.biortech.2021.125698>.
- [108] Yu, F., Li, Y., Huang, G., Yang, C., Chen, C., Zhou, T., Zhao, Y., Ma, J., 2020. Adsorption behavior of the antibiotic levofloxacin on microplastics in the presence of different heavy metals in an aqueous solution. Chemosphere 260, 127650. <https://doi.org/10.1016/j.chemosphere.2020.127650>.
- [109] Yu, Y., Wang, W., Shi, J., Zhu, S., Yan, Y., 2017. Enhanced levofloxacin removal from water using zirconium (IV) loaded corn bracts. Environ Sci Pollut Res 24, 10685–10694. <https://doi.org/10.1007/s11356-017-8700-7>.
- [110] Yuan, N., Gong, X., Sun, W., Yu, C., 2021. Advanced applications of Zr-based MOFs in the removal of water pollutants. Chemosphere 267, 128863. <https://doi.org/10.1016/j.chemosphere.2020.128863>.
- [111] Zhang, Q., Sun, X., Dang, Y., Zhu, J.J., Zhao, Y., Xu, X., Zhou, Y., 2022. A novel electrochemically enhanced homogeneous PMS-heterogeneous CoFe₂O₄ synergistic catalysis for the efficient removal of levofloxacin. J Hazard Mater 424, 127651. <https://doi.org/10.1016/j.jhazmat.2021.127651>.
- [112] Zou, Y., Zhang, R., Wang, L., Xue, K., Chen, J., 2020. Strong adsorption of phosphate from aqueous solution by zirconium-loaded Ca-montmorillonite. Appl Clay Sci 192. <https://doi.org/10.1016/j.clay.2020.105638>.
- [113] Zuo, Q., Gao, X., Yang, J., Zhang, P., Chen, G., Li, Y., Shi, K., Wu, W., 2017. Investigation on the thermal activation of montmorillonite and its application for the removal of U(VI) in aqueous solution. J Taiwan Inst Chem Eng 80, 754–760. <https://doi.org/10.1016/J.JTICE.2017.09.016>.